Expert Systems With Applications 246 (2024) 123167

Contents lists available at ScienceDirect

Expert Systems With Applications

journal homepage: www.elsevier.com/locate/eswa

Wearable wrist to finger photoplethysmogram translation through restoration using super operational neural networks based 1D-CycleGAN for enhancing cardiovascular monitoring

Sakib Mahmud [a,1], Muhammad E.H. Chowdhury [a,2,*], Serkan Kiranyaz [a,3], Malisha Islam Tapotee [b,4], Purnata Saha [b,5], Anas M. Tahir [c,6], Amith Khandakar [a,7], Abdulrahman Alqahtani [d,e,8]

[a] Department of Electrical Engineering, Qatar University, Doha 2713, Qatar
[b] Department of Electrical and Electronic Engineering, University of Dhaka, Dhaka 1000, Bangladesh
[c] Department of Electrical and Computer Engineering, University of British Columbia, 5500 – 2332 Main Mall, Vancouver, BC V6T 1Z4, Canada
[d] Department of Medical Equipment Technology, College of Applied, Medical Science, Majmaah University, Majmaah City 11952, Saudi Arabia
[e] Department of Biomedical Technology, College of Applied Medical Sciences in Al-Kharj, Prince Sattam Bin Abdulaziz University, Al-Kharj 11942, Saudi Arabia

ARTICLE INFO

Keywords:
TTR-GAN
1D-CycleGANs
Super-ONN
Wearables
Blind PPG Restoration
Wrist to Finger PPG Translation
Heart Rate Variability

ABSTRACT

Background and Motivations: Physiological signals, such as the Photoplethysmogram (PPG) collected through wearable devices, consistently encounter significant motion artifacts. Current signal processing techniques, and even state-of-the-art machine learning algorithms, frequently struggle to effectively restore the inherent bodily signals amidst the array of randomly generated distortions. This often leads to the modification or even the degradation of the underlying physiological information.

Methods: To enhance heart rate estimation from wrist PPG (wPPG) signals, this study introduces the Translation Through Restoration GAN (**TTR-GAN**). **TTR-GAN** comprises cascaded dual-stage 1D Cycle Generative Adversarial Networks (1D-CycleGANs) constructed using Super-ONNs. In the first phase, corrupted wPPG waveforms are blindly restored using a 1D-CycleGAN-based restoration framework. Subsequently, in the second phase, the restored wPPG waveforms are translated into clean finger PPG (fPPG) signals through a 1D-CycleGAN-based signal-to-signal translation or synthesis framework. Both the restorer and translator GANs undergo independent evaluation using robust temporal, spectral, and clinical metrics.

Results: The application of the multipass restoration scheme to the wPPG signals resulted in significantly lower entropy compared to the raw wPPGs, indicating reduced irregularity. Using the proposed **PRTX** metric to evaluate the translational ability of the multichannel translator CycleGAN, we achieved a substantial improvement of **35.88%** in wrist-to-finger PPG translation. The correlation between the pulse rate and pulse rate variations estimated from the generated fPPG signals and the heart rate and heart rate variability readings from the ground truth ECG improved by approximately **10.4%** and **14.7%**, respectively, when compared to the raw wPPG signals.

* Corresponding author.
E-mail addresses: sakib.mahmud@qu.edu.qa (S. Mahmud), mchowdhury@qu.edu.qa (M.E.H. Chowdhury), mkiranyaz@qu.edu.qa (S. Kiranyaz), malishaislam-2017814845@eee.du.ac.bd (M. Islam Tapotee), purnata-2017514839@eee.du.ac.bd (P. Saha), anas5@student.ubc.ca (A.M. Tahir), amitk@qu.edu.qa (A. Khandakar), ama.alqahtani@psau.edu.sa (A. Alqahtani).
[1] 0000-0002-4599-2192.
[2] 0000-0003-0744-8206.
[3] 0000-0003-1551-3397.
[4] 0009-0001-3427-5489.
[5] 0000-0003-3818-0572.
[6] 0000-0001-5018-0626.
[7] 0000-0001-7068-9112.
[8] 0000-0002-6658-3240.

https://doi.org/10.1016/j.eswa.2024.123167
Received 27 July 2023; Received in revised form 5 November 2023; Accepted 4 January 2024
Available online 18 January 2024

Conclusion: The proposed **TTR-GAN** can be implemented in wearable devices to obtain reliable real-time cardiovascular data during daily activities.

1. Introduction

Plethysmography is a medical technique used to measure changes in volume within an organ or the entire body. The term "Plethysmography" is derived from the Greek word "plethysmos," which means increasing, enlarging, or becoming full, among other meanings (Plethysmography: Purpose, Procedure & Preparation, 2022). Photoplethysmography (PPG) is an optically obtained plethysmogram, primarily collected from a pulse-oximeter device. It is used to quantify the perfusion of blood to the dermis and subcutaneous tissue of the skin. While PPG is one of the most easily recordable physiological signals, it can be employed to estimate various vital body parameters such as Heart Rate (HR) (Reiss, Indlekofer, Schmidt, & Van Laerhoven, 2019), Respiratory Rate (Pimentel, 2017; Chowdhury, 2022), Blood Oxygen Saturation (SpO2) (Banik, Hossain, Kwon, Kim, & Kim, 2020), and Blood Pressure (BP) (Mahmud, 2022; Chowdhury, 2020). So, among the four vital body parameters, which include body temperature, heart rate, respiration rate, and blood pressure (Vital Signs, 2022), three can be robustly estimated from PPG signals (Reiss et al., 2019; Pimentel, Aug. 2017; Chowdhury, 2022; Banik et al., 2020; Mahmud, 2022; Chowdhury, 2020). Due to its non-invasiveness, ease of acquisition, direct or indirect relation to various vital body parameters, and the ability to be combined with other physiological signals for creating robust solutions (Mahmud, 2022; Mahmud, 2023), there have been several recent studies that utilized PPG and its derivatives to develop various healthcare tools and applications (Mahmud, 2023; Shabaan, et al., 2020; Liu et al., 2018; Yang et al., Nov. 2019; Alonzo and Co, 2018; Han, 2020; Spachos et al., 2011; Reşit Kavsaoğlu et al., 2014). PPG signals have been instrumental in detecting and predicting various cardiovascular anomalies alongside ECG signals (Mahmud, 2023; Shabaan, et al., 2020; Liu et al., 2018). When combined, PPG and ECG signals, or their features, have contributed to the development of robust machine learning tools for estimating cardiovascular diseases (CVDs) such as Heart Rate Variability (HRV) analysis (Liu, Fang, Chen, Li, & Li, 2018), Atrial Fibrillation (AF or A-Fib) detection (Yang et al., 2019), Ventricular Fibrillation (V-Fib) detection (Alonzo & Co, 2018), and Premature Atrial and Ventricular Contraction Detection (Han, 2020), among others. In some studies, PPG has shown promise for Biometric Identification as an alternative to ECG (Spachos, Gao, & Hatzinakos, 2011; Reşit Kavsaoğlu, Polat, & Recep Bozkurt, 2014).

PPG is primarily obtained from fingertips using pulse-oximeter-based sensors in both clinical and non-clinical settings. The shape of PPG signals can vary due to the contact pressure applied to the skin during data collection (Scardulla, D'Acquisto, Colombarini, Hu, Pasta, & Bellavia, 2022). Besides fingers, PPG can also be acquired from other body locations, such as the wrist (Lee, Chung, & Lee, 2019), arm (Zhang, Zhou, & Zeng, 2017), forehead (Wan, Chen, & Yang, 2022), and other areas like the toe or ankle (Ubbink, 2004; Jönsson, Laurent, Eneling, Skau, & Lindberg, 2005), chest (Marzorati, Bovio, Salito, Mainardi, & Cerveri, 2020), and so on. The shape of PPG signals may also differ across different acquisition locations on the body (Hartmann et al., 2019; Chan, 2019; Hartmann et al., 2019); even when collected from the same subject within the same timeframe. Other factors affecting PPG shape, such as patient age (Hartmann et al., 2019; Yousef, Reaz, & Ali, 2022), blood pressure level (Martínez, Howard, Abbott, Lim, Ward, & Elgendi, 2022), or blood glucose level (BGL) (Golap, Raju, Haque, & Hashem, 2021), change very slowly and remain stable for a subject over a long duration, thus seldom impacting real-time setups. However, during real-time data acquisition, replicating studies from PPG acquired from different parts of the body (e.g., finger vs. wrist) presents challenges, as some PPG features change along with their shape. Hartmann et al. (2019) reported that measurement sites significantly varied mean amplitude, peak point position, notch location, and reflective index among PPG signals acquired from six different body locations (finger, upper wrist, lower wrist, arm, earlobe, and forehead). Interestingly, PPG acquired from the lower wrist was found to be more similar to the most abundant finger PPG (fPPG) than the PPG acquired from the upper wrist. Moreover, PPG collected from different regions of the body exhibits phase shifts due to variations in Pulse Transit Time (PTT) resulting from the blood flowing from the aortic valve to the specific location, which was minimized in these studies during experimentation: (Hartmann et al., 2019; Hartmann et al., 2019). Therefore, for vital body parameter estimation, transferring knowledge learned from PPG collected at one physiological location to another is challenging but essential. Nevertheless, finger PPG is considered the gold standard for clinical data acquisition, and most of the large and diverse clinical-grade waveform databases (e.g., MIMIC-III ("MIMIC-III Waveform Database v1.0", 2022; Johnson, 2016)) include fPPG along with other physiological signals such as ECG. However, it is not clinically acceptable to transfer knowledge acquired from training an algorithm on a dataset containing clinical grade fPPG to PPG acquired from another body location using a non-clinical-grade device (e.g., wPPG from wearables) for estimating body parameters due to feature variations and cross-domain challenges. Furthermore, the measured Pulse Rate Variability (PRV) from wPPG signals is less correlated with the ground truth HRV measured from ECG signals than the PRV measured from fPPG signals, as reported by Nardelli, Vanello, Galperti, Greco, & Scilingo, 2020. Paliakaitė (2021) through their experiments showed that wPPG is more erroneous than fPPG for cuff-less, continuous blood pressure estimation. On the other hand, Rajala, Lindholm, and Taipalus (2018) reported a stronger correlation between fPPG and Pulse Wave Velocity (PWV) than wPPG. Beh and Wu (2022) demonstrated that simultaneously collected ECG is the most efficient in classifying the level of mental workload among a group of controlled subjects, closely followed by fPPG, then wPPG. Apart from the presence of severe motion artifacts in wPPG, one primary reason behind these outcomes is the loss of intrinsic features in wPPG compared to fPPG or earlobe PPG, partially due to poor arterial blood supply in those organs (Hartmann et al., 2019). In an attempt to minimize feature loss, Tsai (2021) in their extensive study reintroduced missing features in distorted PPG (finger and wrist), the first derivative of PPG (FDPPG, VPG, or PPG') and the second derivative of PPG (SDPPG, APG, or PPG'') by setting manual thresholds on the third derivative of PPG (TDPPG or PPG''') based on the feature sets of uncorrupted PPG. They disassembled the wPPG and fPPG signals into their component waves or harmonics and showed that the variation in their shapes and features is primarily due to them sharing the same harmonic content (component frequencies) but with varying amplitudes. However, this scheme was not entirely successful due to the existence of missing features even in TDPPG to some extent, which could potentially be resolved using higher-order derivatives. Challenges of this nature can be readily addressed through deep learning-based approaches. A study conducted by the Stanford Machine Learning Group led by Andrew Ng (Voisin, Shen, Aliamiri, Avati, Hannun, & Ng, 2022) demonstrated that during training for AF episode detection from ambulatory PPG, the intermediate kernels in their deep Convolutional Neural Network (CNN) network automatically generated derivatives of PPG while learning. Hence, efficient deep learning approaches, such as Generative Adversarial Networks (GANs) (Goodfellow, 2014), should be capable of effortlessly restoring missing features in corrupted PPG signals. In addition to conventional GANs (Goodfellow, 2014), there exist purpose-

built advanced and hybrid versions of GANs, like DCGAN (Radford, Metz, & Chintala, 2015), StyleGAN (Karras, Laine, & Aila, 2021), Pix2Pix (Lata, Dave, & Nishanth, 2019), DiscoGAN (Kim, Cha, Kim, Lee, & Kim, 2017), LSGAN (Mao, Li, Xie, Lau, Wang, & Smolley, 2017), and CycleGAN (Zhu, Park, Isola, & Efros, 2017), which can be applied for generative adversarial learning, as is the focus of this application. Among these, Cycle Generative Adversarial Networks, or CycleGANs, possess the ability to maintain consistency while learning to transform between images or signals of different modalities. This consistency serves as a crucial rationale behind the interest in CycleGANs for various clinical applications (Armanious et al., 2019). Therefore, in this study, our objective is to utilize CycleGANs to restore these harmonic components and synthesize fPPG from the corresponding wPPG.

As discussed earlier, estimating HR, HRV, and other bodily parameters from PPG signals and making clinical decisions is more challenging and prone to error compared to directly acquiring from ECG. It becomes even more challenging when using wPPGs due to the inherent feature loss even in clean wPPG signals and their increased susceptibility to motion artifacts generated by body movements. In recent years, wearable wPPG has been widely employed to estimate the heart rate of subjects in real-time during their daily activities (Thomas and Gopi, 2019; Biswas, 2019; Chowdhury et al., 2018; Jarchi and Casson, 2017; Zhang et al., 2015; Burrello, 2021; Roy and Gupta, 2020; Fujita et al., 2018; Rocha, Aug. 2020; Panwar et al., 2020; Song et al., 2021; Yen et al., 2022; Yen et al., 2022; Risso, 2021; Ismail et al., 2022). In response to the challenges encountered during data acquisition, feature extraction, and body parameter estimation from wearable devices, several methods have been proposed in these studies. While most of the current research employs various signal processing techniques, the utilization of deep machine learning networks in this field remains relatively limited. CorNet (Biswas, 2019), along with its more efficient version Binary-CorNet (Rocha, 2020), used a combination of simple CNN and Long Short-Term Memory (LSTM) blocks to estimate HR and Biometric Identification from ambulatory PPG. MoDTRAP (Roy & Gupta, 2020) implemented multiple signal processing techniques in conjunction with LSTM and Multilayer Perceptron (MLP) networks for HR estimation from motion-corrupted PPG data. PP-Net, proposed by Panwar, Gautam, Biswas, & Acharyya, 2020, also utilizes a combination of CNN and LSTM to estimate HR and BP from fPPG data collected from the MIMIC-III dataset (MIMIC-III Waveform Database v1.0, 2022; Johnson, 2016). Song, Nam, & Kim, 2021 introduced the NAS-PPG framework for HR estimation from wPPG by combining multiple datasets through neural network search. Yen, Chang, and Liao (2022) and Yen, Liao, and Huang (2022) employed CNN-LSTM networks for the estimation of HR, BP, and other physiological parameters from fPPG signals collected from MIMIC-III. Risso, 2021 presented MorphNet for HR estimation from motion-corrupted wPPG data from the PPG-DaLiA dataset (Reiss et al., 2019). In a very recent study, Ismail, Siddiqi, & Akram, 2022 proposed a Convolutional-Recurrent Regressor model for HR estimation from wPPG signals while correcting motion artifacts using corresponding 3-axis accelerometer (ACC) signals. However, to the best of our knowledge, none of the studies in the current literature have attempted to synthesize fPPG from wPPG for body parameter estimation. This is primarily due to two main challenges: the absence of a dataset containing corresponding fPPG and wPPG for evaluating signal-to-signal translation and the lack of corresponding ground truth ECG data for validating the estimated body parameters. Additionally, the challenge of estimating clean finger PPG directly from corrupted wrist PPG further complicates this task.

CycleGANs used in this study have primarily been applied in two types of applications: image restoration (Wu et al., 2019; Wang et al., 2022; Jia et al., 2019; Peng et al., 2020) and image-to-image translation or transformation, including domain adaptation and synthetic image generation (Dai and Tang,2022; Li et al., 2019; Tang et al.; Wang,2019SPS:id::bib67). There have been some preliminary studies that employed CycleGANs to correct motion artifacts from 1D physiological signals (predominantly wrist PPG) using wearable devices (Long, Kim, Lee, & Chung, 2022; Zargari, Aqajari, Khodabandeh, Rahmani, & Kurdahi, 2022). In these studies, the authors converted the clean and corrupted PPG signals into 2D spectrograms during training and reverted them to 1D signals during the evaluation phase. In an early study, Lin, Zhang, & Liu, 2022 successfully removed Ballistocardiogram (BCG) artifacts from simultaneous EEG-fMRI (Electroencephalography and functional magnetic resonance imaging) signals using a 1D-CycleGAN. Kiranyaz et al. in their pioneering study introduced a 1D Operational CycleGAN-based blind restoration scheme which effectively restored corrupted Holter ECGs regardless of the artifacts and outperformed CNN-based CycleGANs while utilizing five times fewer network parameters. In a more recent study, Mahmud et al. (2024) proposed a supervised, attention-guided operational CycleGAN (AGO--CycleGAN) method to restore motion-corrupted EEG signals. CycleGANs have also been applied to signal-to-signal translation studies, such as the work in (Seo, Yoon, Joo, & Nam, 2022), which generated 12-lead ECG traces from single-channel ECG signals using CycleGANs. Mohebbian et al. (2022) and Basak (2024) reconstructed pure fetal ECG signals from a mixture of mother and fetal ECGs using CycleGANs. Several studies have attempted to generate synthetic EEG signals for data augmentation and other purposes (Hartmann et al., 2022; Xu, 2021; Luo and Lu, 2018; Jiao et al., 2020). More recently, some studies have focused on using cascaded CycleGANs to address challenging problems spanning multiple domains. The R2C-GAN framework, proposed by Ahishali, Degerli, Kiranyaz, Hamid, Mazhar, & Gabbouj, 2022 employed 2D-CycleGANs to blindly restore noisy X-ray images before COVID-19 classification. In contrast, Kanti Podder (2023) introduced a 1D-CycleGAN-based approach to restoring carotid artery flow velocity (cbfv) waveforms, enhancing the performance of a patient classification model. Sayem et al. (2023) in a very recent study proposed a 1D-CycleGAN-based wPPG restoration framework to enhance AF-detection (i.e., classification) from wearables. To the best of our knowledge, no prior study in the 1D domain has explored the cascading of signal restoration and signal-to-signal translation CycleGANs to address any problem, as explored in this study.

In light of the aforementioned challenges associated with extracting physiological parameters from wearable wPPG, this study introduces the Translation Through Restoration (**TTR-GAN**, in short), a dual-stage framework based on 1D-CycleGANs, designed for robustly estimating vital body parameters from wrist-worn wearable devices. As illustrated in Fig. 1, the **TTR-GAN** primarily comprises two cascading 1D-CycleGAN-based sub-systems. The primary objective of the CycleGANs in the first stage is to restore corrupted wPPG signals into clean wPPG signals. This restoration process significantly enhances the overall signal quality by eliminating artifacts that are challenging to remove using conventional signal processing techniques. However, while the clean wPPG signals exhibit improved quality, they may still lack some of the diagnostic or clinical information present in clinical grade fPPG waveforms. To address this, CycleGAN in the second stage transfers the domain of the restored wPPG signals to clinical grade fPPG signals through translation. The PR and PRV extracted from the generated fPPG signals closely correlate with HR and HRV extracted from clinical-grade ECG signals, even more than the restored wPPG signals. The primary contributions of this study are summarized as follows:

- In this pioneering study, clinical-grade fPPG signals are synthesized from restored motion corrupted wPPG data obtained using a wristwatch through the proposed **TTR-GAN** to improve the precision of the estimated physiological information such as heart rate, heart rate variability, etc.
- To the best of our knowledge, this study is the first to blindly restore PPG signals and their derivatives using 1D-CycleGANs.
- This study represents the first instance where 1D-CycleGANs have been cascaded for both signal restoration and signal-to-signal synthesis.

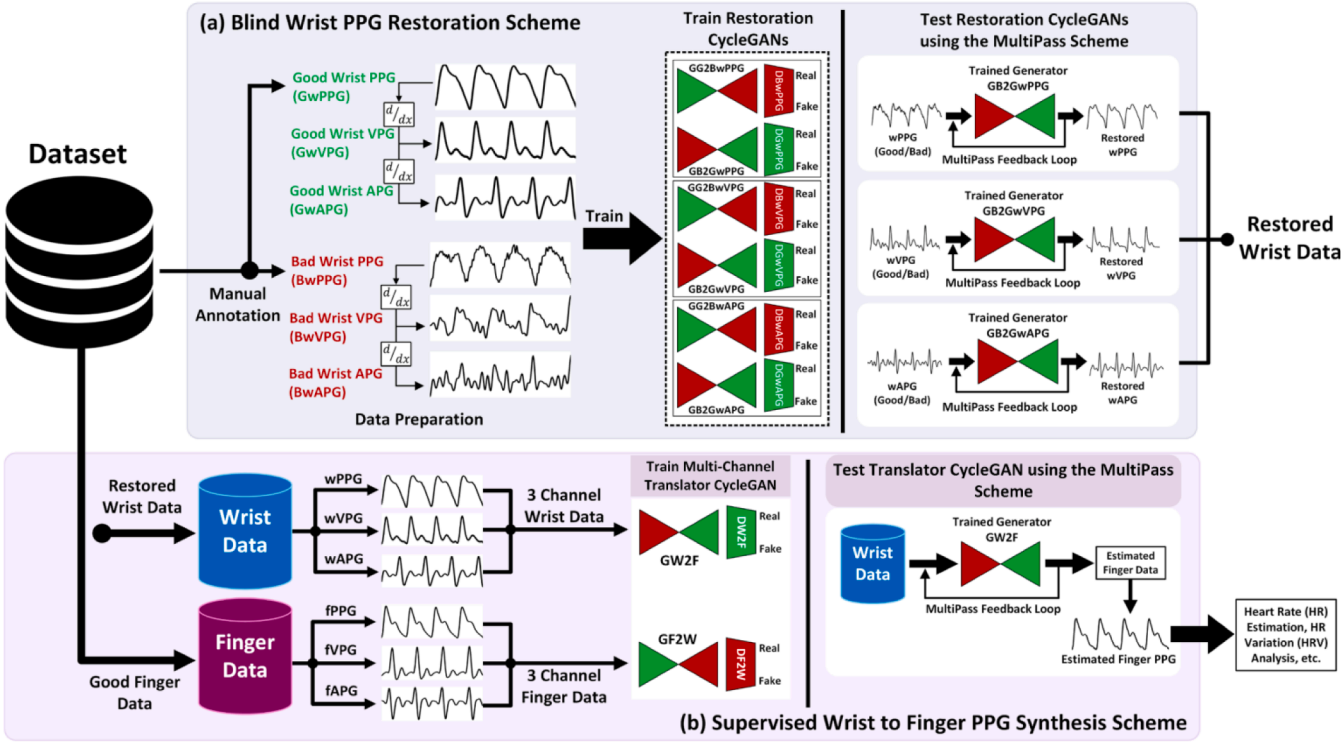

Fig. 1. The proposed TTR-GAN framework (3-channel approach) operates in two phases: **(a)** Initially, the corrupted wPPGs and their first two derivatives are independently and blindly restored using the Restoration or Restorer GANs. **(b)** In the second stage, the restored wPPG data is utilized to translate to fPPG waveforms through the 3-channel Translator GAN. In each stage, the signal restoration or translation performance of the 1D-CycleGANs is assessed both temporally and spectrally. Finally, we conducted a clinical evaluation of the generated fPPGs in comparison to the input raw wPPGs against ground truth ECGs.

- To the best of our knowledge, this study is the first to employ Super Generative Neuron-based Operational Neural Networks (Super-ONNs) in a 1D application.
- For the first time, state-of-the-art time-series entropy measurement techniques have been used to quantitatively evaluate the signal restoration performance of the Restoration GANs. We have introduced the novel PRTX metric to reliably quantify the performance of the Translator GAN in synthesizing fPPG signals from the phase-shifted wPPG waveforms.

The remainder of the paper is organized as follows: In Section 2, we delve into the materials and methods employed in this study, providing a comprehensive overview of the theoretical foundations of Super Generative Neuron based Operational Neural Networks (Super-ONNs) and the architectures of the 1D- CycleGANs used for wPPG restoration and wPPG to fPPG translation. Section 3 includes a concise account of the dataset employed in this study, data preparation techniques, experimental configurations, and an evaluation of the proposed **TTR-GAN** framework's quantitative and qualitative performance. Lastly, in Section 4, we present a succinct conclusion.

2. Materials and methods

In this section, we first review the evolution of non-localized kernel-based 1D Super Generative Neuron Operational Neural Networks (1D-Super-ONNs) in comparison to Convolutional Neural Networks (CNNs), ONNs, and Self-ONNs. Following that, we provide an overview of the general structure and components of the proposed **TTR-GAN** framework, along with an explanation of the evaluation strategies.

2.1. 1D-Super-ONNs: 1D-Self-ONNs infused with super neurons

Conventional CNNs utilize only linear convolutional operators for feature propagation through their neurons and layers. The output of the k^{th} neuron in the l^{th} layer of a 1D-CNN can be expressed as Eq. (1) (Li et al.). In this case, for the sake of simplicity, a convolutional operation with unit stride and zero padding was considered.

$$x_k^l = b_k^l + \sum_{i=0}^{N_{l-1}} x_{ik}^l \tag{1}$$

where b_k^l is the bias associated with the neuron and x_{ik}^l is the l^{th} layer's k^{th} neuron output, which can be further expressed as Eq. (2),

$$x_{ik}^l(m) = Conv1D\left(w_{ik}, y_i^{l-1}\right) \equiv \sum_{r=0}^{k-1} w_{ik}^l(r) y_i^{l-1}(m+r) \tag{2}$$

where w_{ik}^l represents the weight of the kernel connecting the i^{th} neuron of the $(l-1)^{th}$ layer to the k^{th} neuron of the l^{th} layer, y_i^{l-1} represents the $(l-1)^{th}$ layer's i^{th} neuron output, and 'm' and 'r' are convolutional operators. The convolution operation for CNNs is depicted in Fig. 2 (a). In contrast to CNNs, Operational Neural Networks (ONNs) (Kiranyaz, Ince, Iosifidis, & Gabbouj, 2020) are more generalized as they can possess non-linear convolutional operators. Based on the generalized operator formula for ONNs (Eq. (3)), it can be realized that in the case of ONNs, every single neuron can be assigned unique nodal (ψ) and pool (P) operators. Due to this flexibility, ONNs gain the ability to incorporate non-linear transformations suitable for a particular set of problems. The operator formula for ONNs (Eq. (3)) can be visualized in Fig. 2 (b).

$$\overline{x_{ik}^l}(m) = P_k^l\left(\psi_k^1\left(w_{ik}^l(r), y_i^{l-1}(m+r)\right)\right)_{r=0}^{k-1} \tag{3}$$

Even with their heterogeneous nature, conventional ONNs are often not suitable for general applications or cannot reach their full potential due to their exponentially increasing computational overhead in proportion to the network complexity, occurring due to their search for the

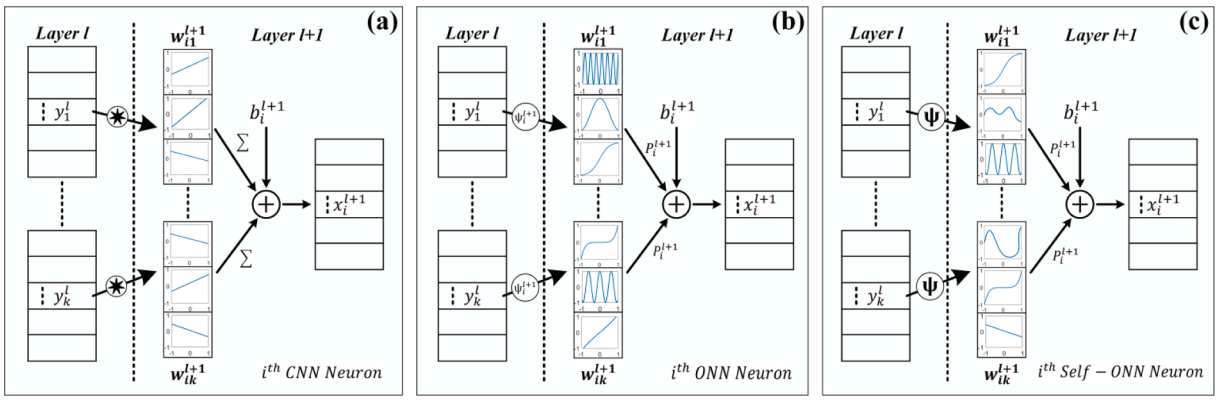

Fig. 2. A depiction of the 1D nodal operations with the 1D kernels of the neurons at layer l for (a) CNN, (b) ONN, and (c) Self-ONN (Kiranyaz et al., 2021).

optimal operator for each neuron. On the contrary, handcrafting a certain set of features for each problem will greatly limit the flexibility and generality of the ONNs. It is also not always possible to express the nodal operator for each neuron in terms of common mathematical functions. To solve this problem, Kiranyaz, Malik, Abdallah, Ince, & Iosifidis, 2021 proposed Self-Generative ONNs, or simply Self-ONNs which use Taylor Series approximation near the origin (a = 0) (i.e., The Maclaurin Series) for the non-linear transformation of each generative neuron, thus allowing any nodal operator function to be formed during training without the need o*f any operator set library or a prior search process. For this reason, Self-ONN-based models can reach an even higher level of diversity and flexibility than static ONNs. Now, as derived in (Kiranyaz et al., 2021; Malik et al., 2021; Malik et al.), the contribution of the i^{th} neuron in generating the feature map x_{ik}^{l} from the $(l-1)^{th}$ layer to the l^{th} layer of a Self-ONN model can be expressed by Eq. (4),

$$\widetilde{x}_{ik}^{l}(m) = \sum_{r=0}^{K-1}\sum_{q=1}^{Q}\widetilde{\psi}_{\mathbf{k}}^{\mathbf{l}}\left(\boldsymbol{w}_{ik}^{l(Q)}(r), y_i^{l-1}(m+r)\right)$$
$$= \sum_{r=0}^{K-1}\sum_{q=1}^{Q}\boldsymbol{w}_{ik}^{l(Q)}(r,q)\left(y_i^{l-1}(m+r)\right)^q \equiv \sum_{q=1}^{Q}\boldsymbol{Conv1D}\left(\boldsymbol{w}_{ik}^{l(Q)}, \left(y_i^{l-1}\right)^q\right) \tag{4}$$

where $\boldsymbol{w}_{ik}^{l(Q)}$ is the K x Q dimensional kernel matrix between the i^{th} neuron from the $(l-1)^{th}$ layer to the k^{th} neuron at the l^{th} layer. This operation has been illustrated in Fig. 2 (c). Here, the hyperparameter Q can be tweaked to control the degree of Taylor series approximation while $\boldsymbol{w}_{ik}^{l(Q)}$ is the learnable kernel, unlike CNNs and ONNs. Finally, the output of a single neuron can be formulated as Eq. (5),

$$\widetilde{x}_k^l = b_k^l + \sum_{i=0}^{N_{l-1}}\widetilde{x}_{ik}^{l} \tag{5}$$

Mentionable that, with the $Q = 1$ setting, a Self-ONN acts like a CNN as there is no non-linearity in the first term of the Taylor Series

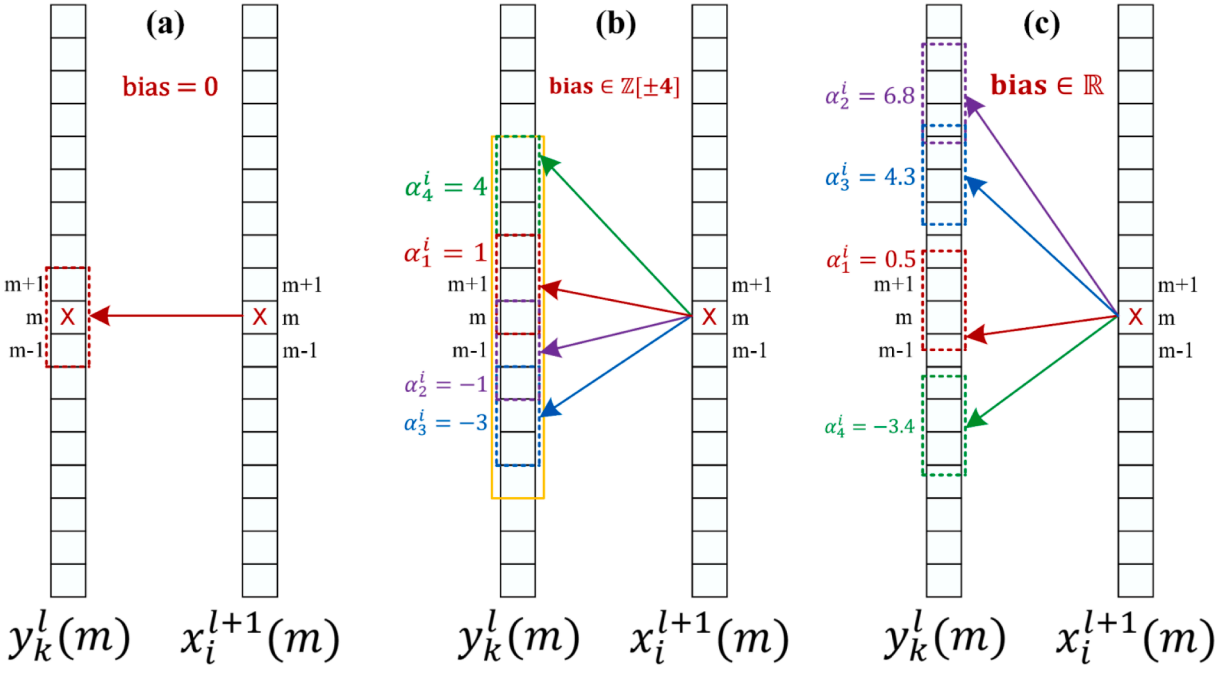

Fig. 3. A Localized **(a)** vs. non-localized kernel operations **(b, c)** to create the pixel, $x_i^{l+1}(m)$, from the output maps of the previous layer neurons; **(b)** Randomly localized kernels within a spatial bias range of $|\Gamma| = 4$ are shown; **(c)** The optimized locations of each kernel during a particular iteration of backward propagation training are illustrated.

approximation.

Nevertheless, Self-ONN like its predecessors (CNN, ONN) contains localized kernel connections between layers. As shown in Fig. 3 (a), for a certain neuron located at a point 'm' at the current layer of a 1D-Self-ONN, all linked kernels in the previous layer are centered at the same location of their output feature map. This limits a neuron to learning from only a fixed location of the previous layer's feature map while the neighboring pixels might also provide important features for the neuron to learn. Kiranyaz et al., in their extensive study (Kiranyaz et al.) proposed two methods to generate non-localized kernels or super neurons to break this limitation. The first approach functions by randomly locating the kernel within a spatial bias of a predefined range (Γ). For this study, let's set the maximum bias range, Γ as 4. Now, for a 1D-Self-ONN model, let $\alpha_k^i \in \mathbb{Z}[\pm\Gamma]$ be the integer bias for the i^{th} neuron of the $(l+1)^{th}$ layer connected to the k^{th} neuron of the l^{th} layer, and $\mathbf{T}^{(\alpha_k^i)}$ be the shift operator for y_k^l by the bias $[\alpha_k^i]$. Then we can perform the shift to obtain $y_k^l(m+\alpha_k^i)$ and operate with the original kernel $\boldsymbol{w}_{ik}^{l+1}$ of size Kx, as expressed in Eq. (6).

$$
\begin{aligned}
x_i^{l+1} &= b_i^{l+1} + \sum_{k=1}^{N_l} oper1D\left(w_{ik}^{l+1}, \overrightarrow{y}_k^{l}{}', NoZeroPad^i\right) \\
\Rightarrow x_i^{l+1}(m)\,\big|_{(0)}^{(M-1)} &= b_i^{l+1} + \sum_{k=1}^{N_l} \left(P_i^{l+1}\left[\psi\left(\overrightarrow{y}_k^{l}(m), w_{ik}^{l+1}(0)\right), \ldots, \psi\left(\overrightarrow{y}_k^{l}(m+r), w_{ik}^{l+1}(r)\right), \ldots\right]\right)
\end{aligned}
\tag{8}
$$

For this study, we have opted for the first approach to generate non-localized kernels for our Super-ONN-based models, given that the Python implementation of the second and more ideal approach is currently unavailable. A comprehensive derivation of forward and backward propagation for Self-ONNs with non-localized Super Neurons or Super-ONNs is provided by Kiranyaz et al., covering both randomized and optimization-based implementations. PyTorch-based implementations of ONNs, Self-ONNs, and Super-ONNs can be found in Kiranyaz, Malik, Gabbouj, & Ince, 2022.

2.2. The Translation Through Restoration GAN (TTR-GAN) framework

$$
\begin{aligned}
x_i^{l+1} &= b_i^{l+1} + \sum_{k=1}^{N_l} oper1D\left(T^{(\alpha_k^i)}\left(y_k^l\right), w_{ik}^{l+1}{}', NoZeroPad^i\right) \\
\Rightarrow x_i^{l+1}(m)\,\big|_{(0)}^{(M-1)} &= b_i^{l+1} + \sum_{k=1}^{N_l} \left(P_i^{l+1}\left[\psi\left(y_k^l(m+\alpha_k^i), w_{ik}^{l+1}(0)\right), \ldots, \psi\left(y_k^l(m+\alpha_k^i+r), w_{ik}^{l+1}(r)\right), \ldots\right]\right) \\
&\forall r \in [0,\ Kx-1]
\end{aligned}
\tag{6}
$$

And, for the kernel element $\boldsymbol{w}_{ik}^{l+1}$, the nodal operator ψ can be expressed as Eq. (7). Upon omitting the DC bias term b_i^{l+1}, the generative neuron has a 2D kernel matrix where the q^{th} weight of the kernel element (r) has been represented by $\boldsymbol{w}_{ik}^{l+1}(r,q)$.

$$
\psi\left(y_k^l(m+\alpha_k^i+r), \boldsymbol{w}_{ik}^{l+1}(r,q)\right) = w_{ik}^{l+1}(r,1)y_k^l(m+\alpha_k^i+r) + w_{ik}^{l+1}(r,2)y_k^l(m+\alpha_k^i+r)^2 + \cdots + w_{ik}^{l+1}(r,Q)y_k^l(m+\alpha_k^i+r)^Q \tag{7}
$$

As shown in Fig. 3 (b), the yellow box represents the preset bias range ($\Gamma = \pm 4$) within which the kernels of size 3 have been shifted randomly, but in integer locations. Now, the i^{th} neuron of the $(l+1)^{th}$ layer can learn from shifted kernels $y_k^l(m+\alpha_k^i)$ in various discrete locations $\alpha_k^i \in \mathbb{Z}[\pm 4]$ within the predefined spatial-bias range.

On the other hand, the second approach consists of guiding the kernels to convergence through backpropagation steps while optimizing along with other parameters during training. In this case, the shift values should be a real number i.e., $\alpha_k^i \in \mathbb{R}$, thus the individual sensitivity $\Delta\alpha_k^i = \frac{\partial E}{\partial \alpha_k^i}$ can be computed. Due to the shift here being a subset of the real numbers, the shifted kernels $\overrightarrow{y}_k^l = \mathbf{T}^{(\alpha_k^i)}y_k^l$ will stay in a fractional grid, as shown in Fig. 3 (c), contrary to the integer grid for the random approach. Thus, Eq. (6) can be replaced with the fractional bias as in Eq. (8). As shown in Fig. 3 (c), the shifted kernels assume fractional positions over the layer y_k^l. A bias range of $\alpha_k^i \in \mathbb{R}[\pm\Gamma]$ can still be predefined, within which the fractional positions can be achieved through interpolation.

The proposed Translation Through Restoration GAN (**TTR-GAN**) framework comprises two schemes: blind wPPG restoration and wPPG to fPPG translation, as illustrated in Fig. 1. The objective is to integrate the restorative and translational capabilities of 1D-CycleGANs within a unified framework. Both schemes follow similar training and testing procedures, except for distinct generator architectures and data preparation steps, as depicted in Fig. 4.

2.2.1. TTR-GAN structure

TTR-GAN first focuses on restoring the corrupted Wrist PPG signals, as generating clinical grade finger PPGs directly from corrupted wPPGs is more prone to error. Additionally, since a majority of the wPPG segments in the dataset were corrupted, using a small subset of good wPPG segments from a limited number of subjects for fPPG translation is insufficient to achieve optimal performance using CycleGANs. wPPG signals, typically generated by wearables, naturally contain more artifacts compared to fPPGs, which are primarily acquired in clinical

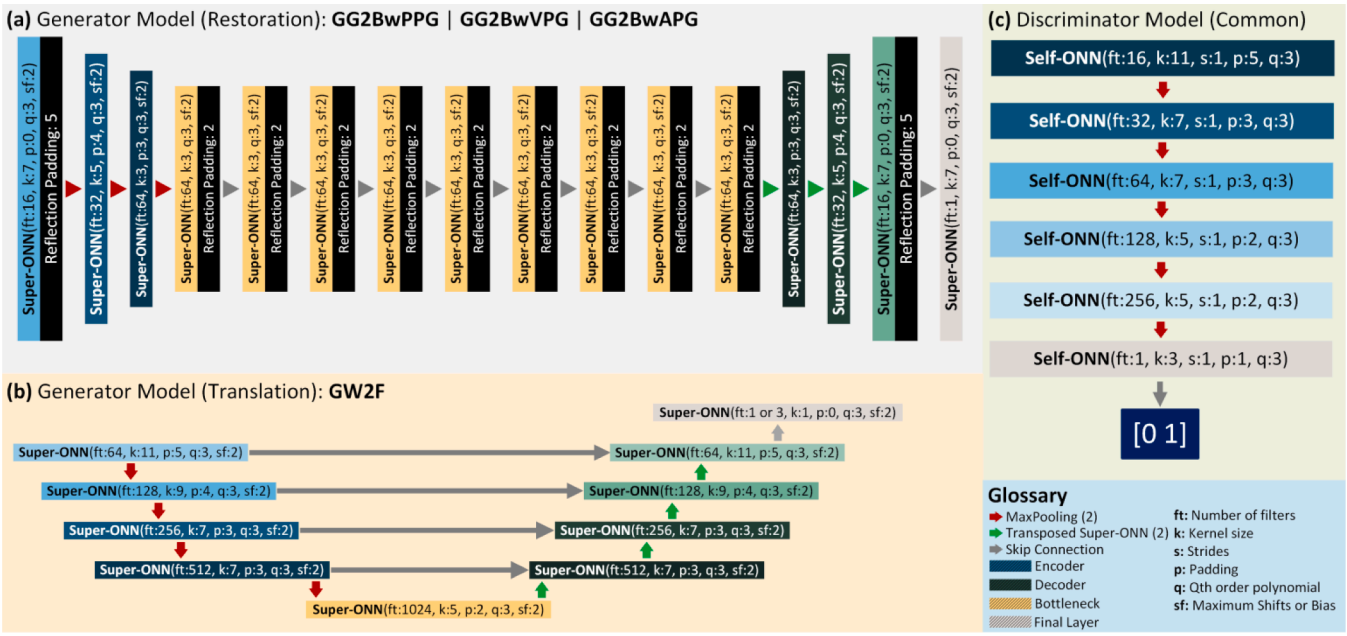

Fig. 4. The Generator and Discriminator architectures for the TTR-GAN framework are as follows: **(a)** The Generator for the Restoration GANs utilizes a ResNet-9block network implemented with Super-ONNs instead of CNNs. **(b)** For the Translation GAN, we employ a Super-ONN-based UNet model. **(c)** Self-ONN-based PatchGAN Discriminators are utilized for both the restoration and synthesis schemes.

settings. These artifacts vary in intensity and type, often diversely affecting wPPGs. In practical terms, it is also more reasonable to restore wPPG signals before synthesizing fPPG signals, considering that in real-life scenarios, wPPG signals are often corrupted by random artifacts. Based on this understanding, we perform unpaired and blind restoration of the wPPG signals in Phase 1 of **TTR-GAN**, carried out by the restorer GANs shown in Fig. 1 (a). This blind restoration scheme, which remains agnostic to the artifacts, enhances the quality and diversity of the clean wPPG subset. Subsequently, we translate all restored wPPG signals into clean fPPGs. As discussed earlier, wPPGs lack diagnostic values compared to clinical grade fPPGs purely due to physiological reasons. So, the translator GAN shown in Fig. 1 (b) is used to generate clinical grade fPPGs from restored, high-quality wPPG signals. Recently Mahmud (2023) have reported improved signal synthesis performance by using the first two derivatives of PPG, namely Velocity of PPG (VPG or FDPPG or PPG') and Acceleration of PPG (APG or SDPPG or PPG"), in parallel to the PPG waveforms. In the case of **TTR-GAN**, we experimented with both single-channel and three-channel approaches and found relatively better performance with the latter. Therefore, in Fig. 1, we propose that **TTR-GAN** should be implemented as a three-channel framework to achieve higher performance. Note that the two additional inputs to the model (wVPG and wAPG) are only used to enhance CycleGAN performance in both phases by incorporating additional features during the learning process. However, when generating metrics (e.g., pulse rate), only PPG signals are utilized. During practical implementations, there is no need for acquiring fPPG or ECG data. We only used ECG for clinical evaluation. Once the **TTR-GAN** has been trained, which requires only wPPG and fPPG data, we deploy the trained restoration and translation models in a cascaded fashion to convert the acquired raw wPPG into clean fPPG.

We utilized a 1D version of the ResNet-based generators commonly employed in 2D-CycleGANs to restore and denoising images (Mostofa et al., 2020; Tavakkoli et al., 2020; Wang and Yang, 2021), as the Restorer GANs. These three-layer deep Restoration GANs incorporate nine residual blocks in the bottleneck layers, with CNN layers being replaced by Super-ONN layers. A detailed illustration is provided in Fig. 4 (a). In the input layer, we employ 8 filters or kernels, which are subsequently doubled to 32 in the bottleneck layer. Each of the nine Super-ONN blocks within the bottleneck includes reflection padding. The kernel size in the initial layer is maintained at 7 to capture coarser features (Kiranyaz et al.), gradually decreasing to 3 in the bottleneck. Conversely, for the generators of the Translator GAN, we employed a five-layer deep UNet (Ronneberger, Fischer, & Brox, 2015) with its CNN layers substituted by Super-ONNs, as depicted in Fig. 4 (b). UNet and its various adaptations have been applied in numerous 2D (Ronneberger et al., 2015; Tahir, 2021; Qiblawey, 2021; Huang, et al., 2022) and 1D (Mahmud, 2023) segmentation tasks over the past few years, making it a suitable choice for the generator in the Translator CycleGAN. The number of filters in the UNet increases from 16 in the initial layer to 256 in the bottleneck. Kernel size and padding decrease as we delve deeper into the model. In both Restoration and Translation GANs, the decoder structure has been designed as the exact reverse of the encoder, except for the final layer. While Restoration GANs always feature a single neuron in the final layer, Translator GANs can have either 1 or 3 neurons depending on the number of channels. For the Super-ONN blocks, we consistently applied a polynomial order *'q'* of 3 in all of our experiments, along with a kernel shifting *'sf'* of 2, as displayed in Fig. 4. Both for restoration and translation, we adopted Self-ONN-based, 5-layer PatchGAN (Isola, Zhu, Zhou, & Efros, 2022) models, as illustrated in Fig. 4 (c). The initial layer comprises 16 filters, with a progressive doubling in the number of filters in each subsequent layer, reaching 256 in the fifth layer before culminating in a binary classifier featuring a linear activation function. The kernel size (from 11 to 3) and padding (from 5 to 1) are diminished in each deeper layer. These discriminators operate as binary classifiers, distinguishing between real and counterfeit or generated samples.

2.2.2. *Strategies for training CycleGANs: restoration vs. translation*

The general approach for training CycleGANs, whether for signal restoration or signal-to-signal translation, remains consistent, except for the data preparation strategies discussed in Section 3.2. The generator's objective is to generate counterfeit samples that closely mimic real ones, while the discriminator's role is to differentiate between authentic and counterfeit samples. Through this adversarial interplay, the CycleGAN continually refines its performance until the generators are capable of producing counterfeit samples of such high caliber that they become

indistinguishable from real samples by the discriminator. In **TTR-GAN**, the Restoration GANs generate counterfeit clean wPPG and its derivatives from the raw waveforms through blind restoration (i.e., restoration irrespective of the artifacts). Conversely, the Translation GAN generates counterfeit fPPG signals based on the restored wPPG waveforms and learns the art of signal synthesis. In this context, for wPPG restoration, the generator *GB2GwPPG* (referred to as the generator for bad to good wPPG restoration) in Fig. 1 (a) gets trained to convert the poor-quality wPPG (W_B) samples into high-quality or good ones (W_G), while the generator *GG2BwPPG* learns to generate W_B from W_G and is discarded after training. Meanwhile, the discriminators *DB2GwPPG* (the discriminator for bad to good wPPG generation, gets trained to discriminate between ground truth and generated good-quality wPPG samples) and *DG2BwPPG* (the discriminator for good to bad wPPG generation) in Fig. 1 (a) strive to maximize the adversarial loss function to create more convincing transformations. The formulations for the adversarial loss functions are provided in Eqs. (9) and (10),

$$Loss_{adv1}(GB2GwPPG, DB2GwPPG, W_B) = \frac{1}{m}\sum_{i=1}^{m}(1 - DB2GwPPG(GB2GwPPG(W_B(i))))^2 \tag{9}$$

$$Loss_{adv2}(GG2BwPPG, DG2BwPPG, W_G) = \frac{1}{m}\sum_{i=1}^{m}(1 - DG2BwPPG(GG2BwPPG(W_G(i))))^2 \tag{10}$$

To enhance the wPPG restoration performance, we incorporate cycle-consistency loss into the Restoration GAN for wPPG, as formulated in Eq. (11).

$$Loss_{cyc}(GB2GwPPG, GG2BwPPG, W_B, W_G) = \frac{1}{m}\sum_{i=1}^{m}(GG2BwPPG(GB2GwPPG(W_B(i)))) - W_B(i)) + \frac{1}{m}\sum_{i=1}^{m}(GB2GwPPG(GG2BwPPG(W_G(i)))) - W_G(i)) \tag{11}$$

The identity loss formulated in Eq. (12) is also considered alongside the above two losses to reduce the variance occurring due to the input sample class being the same as that of the desired output.

$$Loss_{ide}(GB2GwPPG, GG2BwPPG, W_B, W_G) = \frac{1}{m}\sum_{i=1}^{m}((GB2GwPPG(W_G(i)))) - W_G(i)) + \frac{1}{m}\sum_{i=1}^{m}((GG2BwPPG(W_B(i)))) - W_B(i)) \tag{12}$$

For the 3-channel approach involving wVPG and wAPG, the same procedure has been applied. Conversely, when wrist and finger PPGs are denoted as *W* and *F*, respectively, the functional aspects of the Translator GAN (Fig. 1 (b)) can be elucidated by substituting W_B, W_G, *GB2GwPPG*, *GG2BwPPG*, *DB2GwPPG* and *DG2BwPPG* with *W*, *F*, *GW2F* (generator for wrist to finger PPG translation), *GF2W* (generator for finger to wrist PPG translation), *DW2F* (discriminator for wrist to finger PPG translation) and *DF2W* (discriminator for finger to wrist PPG translation), respectively, as shown in Eqs. (9) to (12). Ultimately, the objective of any CycleGAN training session is to minimize the overall loss as formulated in Eq. (13).

$$Loss_{total} = Loss_{adv1} + Loss_{adv2} + \lambda Loss_{cyc} + \beta Loss_{ide} \tag{13}$$

Here, λ and β represent the loss weights that are fine-tuned before training. All losses have been formulated based on the Mean Squared Error (MSE). It's worth noting that for the multichannel Translator GAN, there is no identity loss implemented. On the other hand, we employ our proposed **PRTX** metric (details in Section 2.3.2), which combines Power Ratio and Temporal Cross-Correlation measures, as the validation metric during the training of the Translator GANs. As for the Restoration GANs, we utilize Spectral Correlation (η_{spec}) (Eq. (14)) and spectral Relative Root Mean Squared Error ($RRMSE_{spec}$) (Eq. (15)), as proposed by Zhang et al. (2021) as the validation metrics.

$$\eta_{spec} = 100\left(1 - \frac{1 - \rho(PSD(F), PSD(GX2C(F)))}{1 - \rho(PSD(F), PSD(W))}\right) \tag{14}$$

$$RRMSE_{spec} = \frac{RMS(PSD(F) - PSD(GX2C(F)))}{RMS(PSD(F))} \tag{15}$$

In this context, PSD stands for Power Spectral Density. It's important to note that **PRTX** (power ratio and temporal cross-correlation), being a combination of temporal and spectral metrics, is partially dependent on the temporal alignment of the waveforms under evaluation. Specifically, they should be aligned or exhibit a constant phase shift. This makes PRTX suitable for the Translator GAN, given that the input wPPG, fPPG, and their respective derivatives are aligned (except for a constant phase shift between wrist and finger data, which is addressed through cross-correlation, as discussed in Section 2.3.2). Conversely, the Restoration GANs operate on unaligned data, and therefore, they are assessed using purely spectral metrics such as η_{spec} and $RRMSE_{spec}$, which do not rely on the relative temporal alignment of the waveforms.

2.3. Evaluation process for TTR-GAN

The Restoration and Translation GANs are assessed separately using distinct sets of quantitative metrics. For the restoration scheme, the input data is unaligned, whereas for signal synthesis, it is aligned. Additionally, the Restoration GANs operate with data from a single modality (wPPG), while the Translation GANs are trained on cross-modal datasets (wPPG to fPPG). Therefore, their respective quantitative metrics should be capable of effectively measuring their performance improvements. We conduct both quantitative and qualitative evaluations of the two **TTR-GAN** framework components.

2.3.1. Blind wrist PPG restoration

In this scheme, we restore corrupted wPPG signals using 1D-CycleGANs. The CycleGAN takes two inputs: clean wPPG or its derivatives and corrupted wPPG or its derivatives. It is trained to learn the underlying probabilistic distribution of both sets of training data and how to improve the corrupted segments based on high-quality samples. However, this data is unaligned, meaning that for a particular corrupted wPPG segment, there is no corresponding clean segment that can be temporally assessed (as elaborated in Section 3.2). Implementing a system that can simultaneously acquire the clean version of the

corrupted wPPG signals is not practically feasible, making it impossible to assess the CycleGAN performance using traditional quantitative evaluation metrics such as accuracy, precision, recall, reconstruction error, or correlation coefficients. Therefore, we propose relative quantification metrics, such as entropy, to evaluate CycleGAN's ability to restore corrupted wPPG signals. Entropy is a commonly used scientific concept for assessing anomalies or randomness in a system. Artifacts in physiological signals are anomalies or irregularities that we aim to quantify using various state-of-the-art time-series entropy measurement techniques. For this study, we employed three different entropy metrics: Approximate Entropy (ApEn) (Pincus, Gladstone, & Ehrenkranz, 1991), Sample Entropy (SampEn) (Richman & Moorman, 2000), and Fuzzy Entropy (FuzzyEn) (Chen, Wang, Xie, & Yu, 2007) to quantify the irregularities (or regularities) in the wPPG waveforms before and after restoration. ApEn, which was proposed by Pincus et al., 1991 for quantifying irregularities in physiological signals (e.g., ECG), is defined in Eq. (16):

$$ApEn = \phi^{m}(r) - \phi^{m+1}(r) \tag{16}$$

where, $\phi^{m}(r)$ can be defined as Eq. (17),

$$\phi^{m}(r) = (N-m+1)^{-1} \sum_{i=1}^{N-m+1} ln \bullet C_i^m(r) \tag{17}$$

Here, $C_i^m(r)$ measures the regularity within a given tolerance r, while $\phi^{m}(r) - \phi^{m+1}(r)$ measures the mean stability of those patterns while iterating through the data points. Richman & Moorman, 2000 introduced SampEn as an improvement over ApEn, and it is formulated in Eq. (18):

$$SampEn = -\ln\left(\frac{A^m(r)}{B^m(r)}\right) \tag{18}$$

Here, $A^m(r)$ and $B^m(r)$ are defined in Eqs. (19) and (20), respectively,

$$A^m(r) = (N-m)^{-1} \sum_{i=1}^{N-m} A_i^m(r) \tag{19}$$

$$B^m(r) = (N-m)^{-1} \sum_{i=1}^{N-m} B_i^m(r) \tag{20}$$

In this case, $A_i^m(r)$ and $B_i^m(r)$ quantify the irregularity in the pattern within a given tolerance r for a signal with N data points, while m denotes the length of compared runs of data (i.e., the threshold for checking patterns). r can also be denoted as the filter level or the threshold for detecting irregularities (i.e., any irregularity with an amplitude lower than this will be ignored). Inspired by ApEn and SampEn, Chen et al. (2007) proposed FuzzyEn for estimating time series irregularities and first applied it to characterize surface Electromyography (EMG) signals. FuzzyEn can be formulated by Eq. (21) as follows:

$$FuzzyEn = \ln(\phi^{m}(n,r)) - \ln\left(\phi^{m+1}(n,r)\right) \tag{21}$$

ϕ^{m} in the FuzzyEn can be defined as Eq. (22),

$$\phi^{m}(n,r) = (N-m)^{-1} \sum_{i=1}^{N-m} \left((N-m-1)^{-1} \bullet \sum_{j=1, j\neq 1}^{N-m} D_{ij}^m \right) \tag{22}$$

Here, D_{ij}^m denotes the degree of similarity or regularity between two adjacent vectors X_i^m and X_j^m. The distorted wPPG signals and their derivatives are generally more irregular, resulting in a higher overall entropy. The contained entropy of the restored wPPG waveforms should be lower due to their uniformity. From Fig. 1 (a), we adopt the multipass evaluation strategy from Kiranyaz et al. through passing the CycleGAN outputs through the trained model multiple times to achieve better wPPG restoration performance. We qualitatively and quantitatively assess the outcomes from each pass in Section 2.3.3 to show that the restoration performance indeed improves until a certain pass starts to show a drop in performance. We use the restored wPPGs from the optimal pass for wPPG to fPPG translation.

2.3.2. Wrist-to-finger PPG synthesis

The wrist-to-finger PPG synthesis scheme is similar to traditional 1D-segmentation model-based signal-to-signal translation (Mahmud, 2023). In the single-channel approach, we train a 1D-CycleGAN to estimate fPPGs from the restored wPPGs. In the three-channel approach (Fig. 1), we include restored wVPGs and wAPGs from phase 1 as inputs to a multi-channel (three-channel) 1D-CycleGAN for fPPG synthesis. In this case, we propose our novel **PRTX** metric due to the shortcomings in the existing metrics for robustly quantifying the performance of the 1D-CycleGANs in wrist-to-finger PPG translation. Initially, we attempted to apply the Pearson Correlation Coefficient (PCC) (Eq. (23)), which failed to evaluate the fPPG translation performance effectively due to its susceptibility to existing phase shifts between the ground truth and the generated fPPG signals (Mahmud, 2023).

$$PearsonCorrelationCoefficient, \rho(x,y) = \frac{\sum_{i=1}^{n}(x_i-\bar{x})(y_i-\bar{y})}{\sqrt{\sum_{i=1}^{n}(x_i-\bar{x})^2}\sqrt{\sum_{i=1}^{n}(y_i-\bar{y})^2}} \tag{23}$$

Even though the generated fPPG signals matched in shape, there was a time domain shift compared to the ground truth due to the phase shift between the input wPPG and fPPG waveforms (Hartmann et al., 2019; Hartmann et al., 2019). Therefore, we utilized cross-correlation (*Xcorr*) for the temporal or time domain evaluation of fPPG translation, as it is insensitive to phase shifts owing to its use of convolution (Bracewell, 1999; Papoulis, 1994). The convolutional operation can be formulated as shown in Eq. (24).

$$f^{*}g = \int_{-\infty}^{\infty} f(\tau)g(t-\tau)d\tau \tag{24}$$

Based on this, the temporal Xcorr (*TXcorr* in this study) between the ground truth and the translated fPPGs can be formulated as in Eq. (25) (Cross-correlation, 2022);

$$\begin{aligned} TXcorr(fPPG, fPPG^{'}) &= \overline{fPPG}^{*} fPPG^{'} \Rightarrow [TXcorr(fPPG, fPPG^{'})](t) \\ &= \int_{-\infty}^{\infty} (\overline{fPPG}(-\tau) \bullet fPPG^{'}(t-\tau))d\tau \\ &\equiv \int_{-\infty}^{\infty} (\overline{fPPG}(\tau) \bullet fPPG^{'}(t+\tau))d\tau \end{aligned} \tag{25}$$

Here, fPPG$^{'}$ represents the translated fPPG from wPPG, and $\overline{\text{fPPG}}$ denotes the complex conjugate of the fPPG signal. However, during the evaluation stage, it was observed that using *TXcorr* alone as a metric did not yield distinguishable results before and after translation. Therefore, we also incorporated the power ratio (PWRR) of the signals into our evaluation metric due to its capacity to quantify the power contained within wPPG and generated fPPG signals, allowing for differentiation. PR can be formulated based on Eq. (26).

$$PowerRatio(PWRR) = 1 - \left(\frac{|P_{norm}(fPPG) - P_{norm}(\overline{fPPG})|}{\max(P_{norm}(fPPG), P_{norm}(\overline{fPPG}))} \right) \tag{26}$$

Here, $max(A,B)$ denotes a built-in function used to determine the maximum value between two variables. This metric has been designed to vary between 0 and 1. Now, the normalized power is denoted as P_{norm}, of a signal x can be defined as shown in Eq. (27).

$$P_{norm}(x) = \frac{\sum_{i=1}^{n}(x_i)^2}{n} \tag{27}$$

Here, n represents the number of data points in the signal. Therefore, the final PRTX metric for evaluating the translation from wPPG to fPPG has

been formulated as the mean of the temporal cross-correlation (TXcorr) and the power ratio (PWRR), as presented in Eq. (28).

$$PRTX = \frac{PWRR + TXcorr}{2} \tag{28}$$

2.3.3. Clinical evaluation process

The proposed **TTR-GAN** (Fig. 1) is a framework for signal restoration and synthesis, particularly for wPPG signals. It cannot detect the QRS complex (R-peaks) from the ECG signals nor the systolic/diastolic peaks from the PPG signals. To clinically evaluate the platform through heart rate (HR) and heart rate variation (HRV) analysis, external tools or algorithms are required. As explained in the introductory section, HR and HRV can be robustly estimated from the ECG signals, while the inverse of the pulse-pulse interval (PPI) from PPG can be used as a pseudo-HR, namely pulse rate (PR). HR is one of the four vital bodily parameters (Vital Signs, 2022), and HR and HRV can be used to reliably predict various cardiovascular diseases (Perret-Guillaume, Joly, & Benetos, 2009), respiratory tract infectious diseases (e.g., COVID-19 (Hasty, García, Dávila, Wittels, Hendricks, & Chong, 2021), hypertension (Chowdhury, 2020; Lan, Raknim, Kao, & Huang, 2018), and more. Resting state HR varies from person to person and can be affected by factors such as stress, anxiety, medication, hormones, high body temperature, dehydration, and physical activity (Olshansky, Ricci, & Fedorowski, 2022). An abnormality in HR and HRV (too high, too low, or irregular) can indicate cardiac complexities, such as Tachycardia (resulting from a high resting HR) (Swai, Hu, Zhao, Rugambwa, & Ming, 2019) and Bradycardia (resulting from a low resting HR) (Mason & Lönnqvist, 2015). In addition to respiratory tract diseases, as discussed earlier (e.g., COVID-19), abnormalities in HR and HRV might also be related to infectious diseases such as viral myocarditis (Schultz, Hilliard, Cooper, & Rihal, 2009), Lyme disease (Lelovas, Dontas, Bassiakou, & Xanthos, 2008), etc. The existence of endocrine disorders, such as Hyperthyroidism (Cacciatori, 1996) and Hypothyroidism (Herrmann, 2020), can also be predicted from abnormally fluctuating HR. Beyond that, HR has direct correlations with the psychological conditions of patients, such as anxiety and depression (Gorman & Sloan, 2000). Recent studies have applied advanced machine learning techniques to link HR and HRV to seemingly unrelated diseases, including Diabetes Mellitus (DM) (Ewing, 1981), inflammation (Williams, 2019), and more. Given this discussion, it is crucial to robustly estimate HR and HRV from wearables in order to monitor such diseases in real-time during 24-hour home monitoring.

In this study, we detect the R-peaks using the deep learning-based R-peak detector proposed by Gabbouj, 2022, which is implemented using a 1D-Self-ONN-based UNet (Ronneberger et al., 2015). It is trained on the benchmark CPSC-2020 ECG dataset (Cai, 2020), which contains more than 1 million beats. Based on the detected R-peaks, we calculate the beat-to-beat, i.e., the RR-interval (RRI or RR-I in short) between the peaks. Mean RR ($\overline{RR}$) and mean HR ($\overline{HR}$) for each segment are estimated using Eqs. (29) and (30), respectively (Qin, Li, Huang, & Zhao, 2017).

$$\overline{RR} = \frac{\sum_{i=1}^{N} RR_{i+1}}{N} \tag{29}$$

$$\overline{HR} = \frac{\sum_{i=1}^{N} \left(\frac{60000}{RR_{i+1}}\right)}{N} \tag{30}$$

Here, RRI is a measurement of the time elapsed between two successive R-waves of the QRS signal on the ECG, typically expressed in milliseconds (ms), while HR, its reciprocal, is generally expressed as beats per minute (BPM). To convert $\overline{RR}$ into $\overline{HR}$ (i.e., converting milliseconds into minutes), Eq. (30) is applied to each RRI-estimate. Pulse rates (PRs) are calculated from the PPI (in place of RRI) using Eqs. (29) and (30) based on the systolic/diastolic peaks extracted from wPPG and fPPG signals using MATLAB-based (Peak analysis, 2023) peak detector used in these studies: (Mahmud, 2022; Mahmud, 2023). We then calculate the Pearson Correlation Coefficient (PCC) (Eq. (23)) between the true HR from ECG and the pseudo-HR or PR from wPPG and synthesized fPPG (fPPG') signals, respectively, over the entire dataset. HRV and PRV are measured per ECG and PPG segment, respectively, using the Root Mean Square of Successive Differences (RMSSD) and per subject using the Standard Deviation of Normal-R-to-Normal-R Intervals (SDNN) (Qin et al., 2017). SDNN and RMSSD can be calculated as shown in Eqs. (31) and (32), respectively.

$$SDNN = \sqrt{\frac{\sum_{i=1}^{N} (RR_i - \overline{RR})^2}{N}} \tag{31}$$

$$RMSSD = \sqrt{\frac{\sum_{i=1}^{N} (RR_{i+1} - RR_i)^2}{N-1}} \tag{32}$$

So, SDNN is determined based on the mean RR ($\overline{RR}$), while RMSSD is akin to a moving average. In this study, we calculate $\overline{RR}$ per subject to measure SDNN. RMSSD, being a dynamic parameter, is divided by one less than the number of RR estimates per segment. SDNN and RMSSD are then averaged over the entire dataset (subject and segment-wise, respectively) to generate a single numerical value (ECG, wPPG, fPPG, and fPPG') for comparison. To conduct a comprehensive analysis, in Section 3.3.3, we create scatter plots to illustrate the correlations between PPI from fPPG vs. wPPG (Fig. 6 (e)) and fPPG' (Fig. 6 (f)). Additionally, we present the trends of HR/PR, RRI/PPI, and HRV/PRV across the entire dataset (Fig. 6 (a-d)). SDNN and RMSSD measures for PRV are calculated based on PPI (instead of RRI) using Eqs. (31) and (32), respectively.

3. Experimentation and results

In this section, we will first discuss the **M**ental Workload **A**ssessment on the N-back Task **U**sing the Wearable **S**ensor (MAUS) dataset (Beh & Wu, 2022; Beh, Yi-Hsuan, & An-Yeu (Andy) Wu, 2021), which was utilized in this study. Second, we will delve into the data preparation strategies and experimental setup that were established for the proposed **TTR-GAN**. Third, we will present detailed quantitative and qualitative assessment results for both wPPG restoration and wrist-to-finger PPG synthesis. Additionally, we will examine the computational complexities of the **TTR-GAN** framework when implemented in a wearable system. Finally, we will conclude this section with a comparative analysis of **TTR-GAN** against relevant frameworks from the literature.

3.1. Mental workload assessment on N-back task using wearable sensor (MAUS) dataset

The MAUS dataset utilized in this study was curated and shared by Beh and Wu (2022) and Beh et al. (2021) to assess mental workloads through physiological signals acquired from wearable devices. This dataset includes wPPG signals obtained wirelessly using a PixArt wristwatch with a sampling frequency of 100 Hz. Additionally, it encompasses fPPG, ECG, and Galvanic Skin Response (GSR) signals, all of which were simultaneously collected using a ProComp Infiniti device with a sampling frequency of 256 Hz (Bio-medical.com, 2022). The dataset was compiled from 22 healthy young participants with a mean age of 23 years and a standard deviation (SD) of 1.7 years. During data collection, each subject was engaged in tasks spanning various levels of mental workload, ranging from restful states to intensive cognitive activities. The average duration of signal acquisition per subject amounted to approximately 35 min, resulting in a total usable signal length of around 12 h and 50 min. The primary motivation behind selecting the MAUS dataset for this study stems from the scarcity of publicly available or shareable datasets that contain concurrent wrist and finger PPG

waveforms suitable for signal-to-signal translation or synthesis, as well as ground truth ECG data for the validation of certain physiological parameters derived from the PPG signals. Notably, none of the similar datasets (Markova et al., 2019; Albuquerque, 2020; Mijić et al., 2019; Vollmer et al., 2023; Gjoreski, 2020) encompass simultaneous recordings of wrist and finger PPG signals. While there have been datasets (Tsai, 2021) that collected concurrent wrist and finger PPG signals, they lacked ECG ground truth, and their accessibility was restricted due to privacy concerns. It is worth mentioning that the GSR signals within the MAUS dataset were not utilized in the context of this study.

3.2. Data preparation and experimental setup

The MAUS dataset included signals collected from two devices, PixArt and ProComp Infiniti, with different sampling frequencies (100 Hz and 256 Hz, respectively). To ensure temporal alignment in the processed dataset, all signals were resampled to a common sampling rate of 125 Hz. Both devices were affected by 50 Hz powerline noise, with PixArt being more severely affected. To reduce powerline noise, a 50 Hz notch filter with a quality factor (Q-factor) of 10 was applied to signals from both devices. Bandpass filters were used to clean the PPG signals, with cutoff frequencies of 0.05 and 30 Hz (Pilt et al., 2013), while the cutoff frequencies for the bandpass filter applied to the ECG signals were 0.1 and 40 Hz (Bailey, 1990). Following practices from similar studies, the signals were segmented into segments of 512 data points, and each segment was normalized to a range between 0 and 1 for preparing the dataset for training deep learning models (Mahmud, 2022; Mahmud, 2023; Ibtehaz, 2022). A total of 8976 segments were extracted from the dataset. Upon meticulous visual assessment of several samples, it was evident that the fPPG and ECG signals were of high quality and did not necessitate restoration. This study conducted experiments using both single-channel (PPG) and three-channel (PPG, VPG, and APG) approaches. For the three-channel approach, VPG and APG signals for both wPPG and fPPG segments were derived and stored in the database (Fig. 1). The extraction and preprocessing of VPG and APG signals, including filtering, alignment, and normalization, followed the process explained in past studies (Mahmud, 2022; Mahmud, 2023). The deep learning networks (CycleGANs) were trained in a Python environment, utilizing an end-to-end pipeline built on the PyTorch library. Each network was trained on an NVIDIA 3080Ti GPU for 1000 epochs while monitoring the validation metrics (η_{spec} and $RRMSE_{spec}$) discussed in Section 2.2.2.

3.2.1. Blind wrist PPG restoration

For the "Blind wPPG restoration" scheme, the wPPG segments were manually categorized into three groups: high, mediocre, and low quality. The annotators rigorously distinguished between high and low-quality wPPG segments, adhering to the data preparation strategies proposed by Kiranyaz et al.. To create an adversarial dataset, the very high-quality wPPG signals were labeled as 'good,' and the very low-quality wPPG signals were labeled as 'bad,' while the rest were categorized as 'mediocre.' During the manual sorting process, certain corrupted segments with NaN values, straight lines, or no discernible physiological information were excluded from the dataset. Out of the 8976 segments, 1876 were labeled as 'good,' 2732 as 'mediocre,' 4204 as 'bad,' and 164 as 'corrupted.' Due to the dataset's class imbalance, the 'good' samples were intentionally overlapped by 50 %, resulting in a final count of 3752 segments. These 3752 'good' segments, along with the 4204 'bad' quality wPPG segments, were utilized to construct 5-fold subject-independent datasets for Cross-Validation (CV). In each fold, all segments (including 'good,' 'mediocre,' and 'bad') from 4 to 5 subjects (approximately 20 % of all subjects) were designated for testing, while the 'good' and 'bad' segments from the remaining subjects were designated for training. As previously explained, the test sets for the restoration GANs did not contain ground truth clean segments, making it impossible to perform a direct quantitative evaluation of the restoration performance in the temporal domain. The annotations for the 'good' and 'bad' wVPG and wAPG segments followed the same criteria as the wPPG segments and were restored independently for the three-channel approach, with configurations similar to those used for wPPG

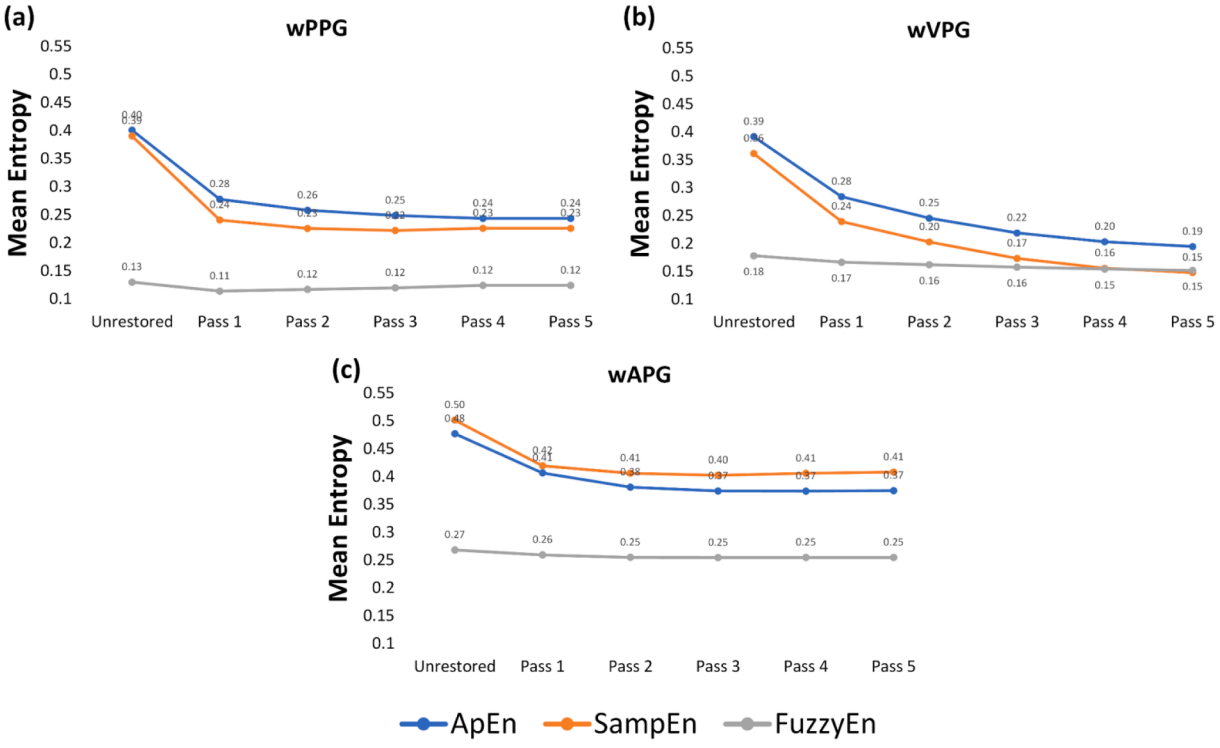

Fig. 5. Entropy measurements for **(a)** wPPG, **(b)** wVPG, and **(c)** wAPG signals before and after restoration, following the multipass restoration scheme in TTR-GAN Phase 1, as depicted in Fig. 1 (a).

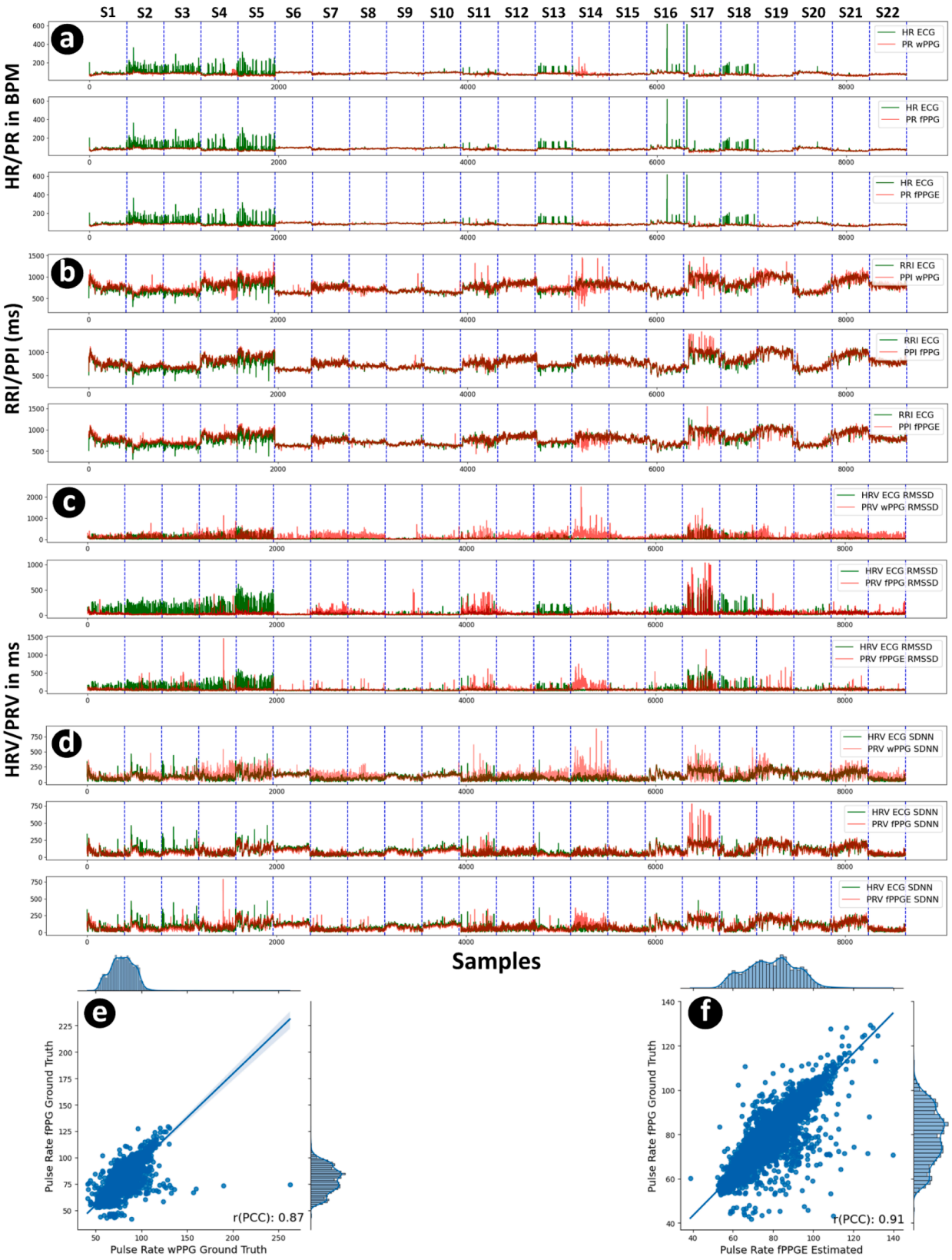

Fig. 6. **(a)** Heart (or Pulse) Rate (HR/PR), **(b)** RR (or PP)-interval (RRI/PPI), Heart (or Pulse) Rate Variability (HRV/PRV) trends in terms of **(c)** RMSSD and **(d)** SDNN based on the ground truth wPPG, fPPG, and estimated fPPG' (fPPGE) against the ground truth ECG are displayed over the entire dataset, with the samples corresponding to each subject annotated. We used an alpha of 65% to create semi-transparent PPG plots. Additionally, **(e)** and **(f)** feature scatter plots illustrate the correlation between PRs extracted from wPPG and fPPG' against those of fPPG, respectively. We noticed a 4% improvement in correlation and rectification of outliers by passing the wPPG signals through TTR-GAN.

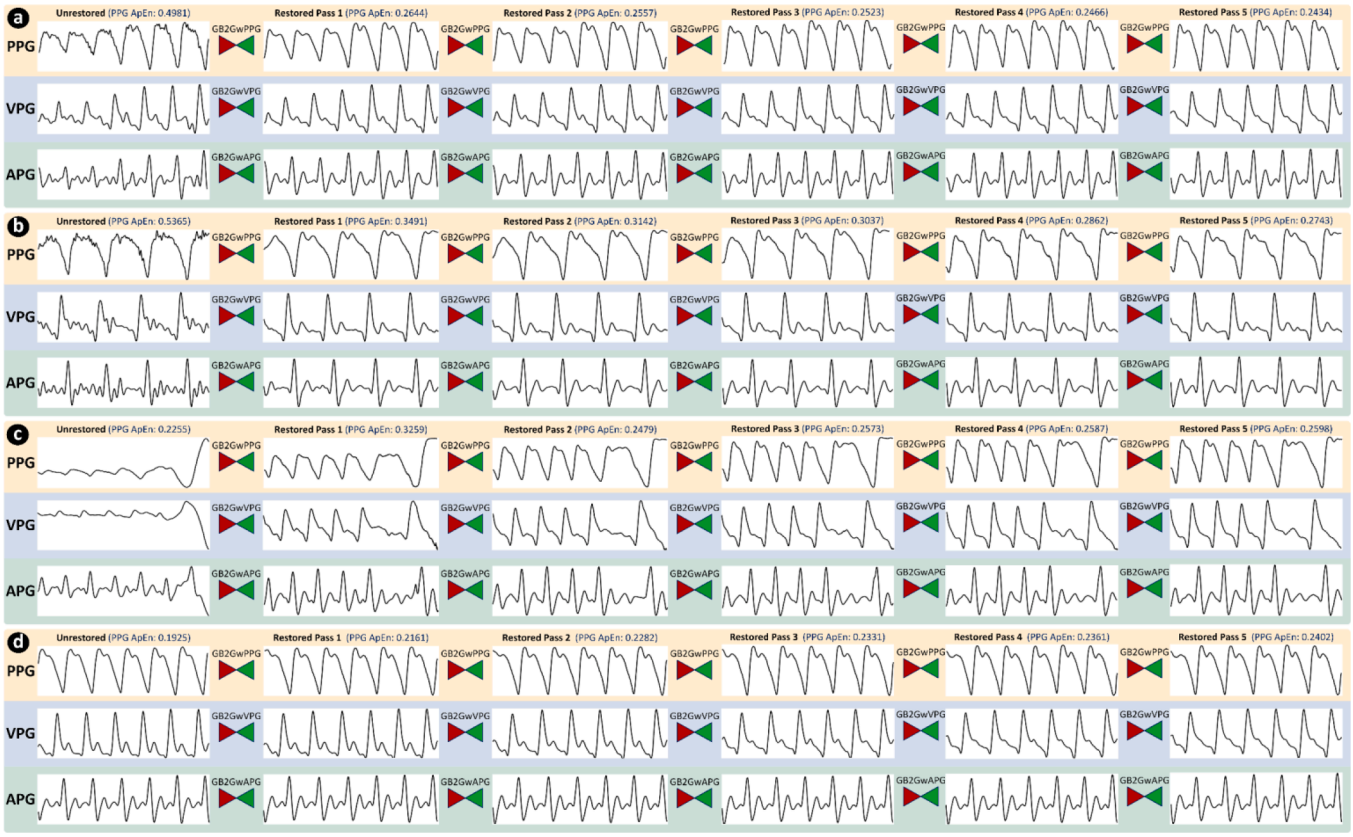

Fig. 7. Qualitative visualization of sample outcomes from the multipass wPPG restoration scheme under TTR-GAN. It includes common cases in which **(a)-(b)** entropy decreased, **(c)** entropy increased, and **(d)** entropy remained similar after wPPG, wVPG, and wAPG restoration. For each sample, we also provide the Approximate Entropy (ApEn) for the wPPG segment before and after restoration.

restoration (as shown in Fig. 1). This approach allowed the three restoration GANs to independently learn the transformation domains for restoring wPPG and its derivatives, which would subsequently be used in the wPPG to fPPG translation phase. During training, 10 % of the segments were randomly selected for validation. Supplementary **Table S1** provides additional details about the folds.

3.2.2. *Wrist-to-finger PPG synthesis*

On the other hand, for the "w2fPPG synthesis" scheme, we employed corresponding wPPG and fPPG segments for one-to-one translation. The restored wPPG segments obtained from all test folds in the previous step were aggregated to form the restored wPPG dataset. Consequently, a total of 8812 segments (comprising 1876 'good,' 2732 'mediocre,' and 4204 'bad' quality wPPG segments) and their corresponding fPPG segments were utilized to train the translator GAN. In the three-channel approach, the wPPG segments constituted just one of the three input channels for the Translator GAN. The other two channels received inputs from the restored wVPG and wAPG segments (as depicted in Fig. 1). The data for training the Translator GAN was partitioned into 5-fold subject-independent CV, adhering to the same approach as that of the restoration GANs. During the training process, 10 % of the segments were randomly selected for validation. In contrast to the restoration scheme, the test sets, in this case, included ground truth fPPG signals and their derivatives, allowing for direct quantitative evaluation in the temporal domain. Further details about the folds can be found in Supplementary **Table S2**.

Table 1
The overall 5-fold-CV w2fPPG translation performance based on the proposed PRTX metric. We also show the performance before and after wPPG restoration.

Metric	Waveform	Before wPPG Restoration		After wPPG Restoration	
		Single Channel	Three Channels	Single Channel	Three Channels
TXcorr	fPPG vs. wPPG	0.6762	0.6762	0.6706	0.6706
	fPPG vs. fPPG′	0.9006	0.9235	0.9466	0.9561
PWRR	fPPG vs. wPPG	0.5440	0.5440	0.5304	0.5304
	fPPG vs. fPPG′	0.8689	0.9238	0.9322	0.9398
PRTX	fPPG vs. wPPG	0.5977	0.5977	0.5867	0.5867
	fPPG vs. fPPG′	0.8953	0.9212	0.9357	0.9455

3.3. *Quantitative evaluation*

In this section, we conduct a quantitative evaluation of the performance of CycleGANs in wPPG restoration and wrist-to-finger PPG translation.

3.3.1. *Blind wrist PPG restoration*

As mentioned earlier, each segment in the processed dataset comprises $N = 512$ data points. For all entropy measurement techniques, we employed an m of 2 and a r of 0.1 (Eqs. (16) to (22)), which are standard values established in the literature (Bandt & Pompe, 2002; Porta, 1998). According to the literature, the value of m should be chosen such that N falls between 10^m and 30^m to ensure reliable measurement of irregularity, a criterion that was satisfied with our selected values. We opted for a small value of r to account for even minor irregularities present in the signals (see Fig. 7). We computed the mean entropies of the 8812 wPPG segments both before and after restoration across all 5 passes. It is important to note that the unrestored data comprises a mixture of corrupted, mediocre, and high-quality signals. The restoration GANs bolstered the approach by preserving the integrity of high-quality wPPGs, wVPGs, and wAPGs for most cases (as depicted in Fig. 7 (d)). Consequently, the entropy measurements remained very close in such

Table 2
PCC between HR extracted from ground truth ECG, wPPG, fPPG, and translated fPPG′ signals for the 3-channel approach.

Parameter	Waveforms	Pearson Correlation Coefficient (PCC)
Heart Rate (HR) vs. Pulse Rate (PR)	ECG vs. wPPG (unrestored)	0.7968
	ECG vs. wPPG (restored)	0.8304
	ECG vs. fPPG	0.9242
	ECG vs. fPPG′	0.9003
Heart Rate Variability (HRV) vs. Pulse Rate Variability (PRV) in SDNN	ECG vs. wPPG (unrestored)	0.6991
	ECG vs. wPPG (restored)	0.7438
	ECG vs. fPPG	0.9254
	ECG vs. fPPG′	0.8457

instances. For mediocre cases, slight improvements were observed, while severely corrupted segments exhibited significant enhancements in entropy measurements (Fig. 7 (a-c)). Fig. 5 presents the average entropy results of 5-fold-CV for wPPGs, wVPGs, and wAPGs before and after restoration.

From Fig. 5, using all techniques, it is evident that the entropy of the waveforms significantly decreased after restoration, indicating the removal of irregularities through the process. It can also be observed that, in most cases, the optimal performance is achieved during the 3rd pass. Beyond the 3rd pass, the improvement is generally negligible, absent, or even leads to degradation in some cases. Consequently, we opt for using the restored wPPG signals from the 3rd pass for the wPPG to fPPG translation phase. It is worth mentioning that for a small group of corrupted segments, the entropy increased after restoration (as shown in Fig. 7 (c)), as these corrupted segments were less irregular compared to the restored ones. These segments belong to the final segments in their respective records and are unique cases specific to this dataset. The MATLAB implementation of the entropy algorithms was sourced from (Monge-Álvarez, 2022).

3.3.2. Wrist-to-finger PPG synthesis

We assessed the translation performance of the 1D-CycleGAN with and without wPPG restoration in both single and three-channel approaches, using the proposed **PRTX** metric. The aggregated 5-fold cross-validation results for w2fPPG translation can be found in Table 1. For a more detailed breakdown, per-fold results with and without wPPG restoration are available in Supplementary Tables S3 and S4, respectively.

From Table 1, we can observe that the **PRTX** between the ground truth fPPG and the fPPG′ (generated fPPG) significantly improved after wPPG restoration. Furthermore, introducing wVPG and wAPG (in the 3-channel approach) to the system led to a slight enhancement in the **PRTX** metric. For the best case, the **PRTX** metric improved from approximately 58.67 % (between fPPG and wPPG) to over 94.55 % (between fPPG and fPPG′) after translation i.e., around **35.88 %** improvement. These results demonstrate the capability of these metrics to effectively quantify the morphological differences between wPPG and fPPG signals and the improvements achieved after translation, irrespective of phase shifts.

Table 3
Mean Heart (or Pulse) Rate (HR/PR), mean RR/PP-Interval (RRI/PPI), and Heart (or Pulse) Rate Variability (HRV/PRV) analysis outcomes over the entire dataset (3-channel) for ECG, wPPG, fPPG, and fPPG'.

Waveforms	Mean HR/PR (BPM)	Mean RRI/PPI (ms)	Mean HRV/PRV (SDNN-ms)	Mean HRV/PRV (RMSSD-ms)
ECG	82.240	770.245	94.008	44.928
wPPG	78.114	789.596	96.048	52.988
fPPG	79.307	751.418	90.489	37.609
fPPG′	79.433	752.274	91.694	41.690

3.3.3. Clinical evaluation: Heart rate and heart rate variability analysis

As previously mentioned, the **TTR-GAN** framework cannot independently determine heart rate (HR), heart rate variability (HRV), pulse rate (PR), and pulse rate variability (PRV) from ECG and/or PPG signals. Its primary function is to enhance corrupted wearable wPPG signals and translate them to clinical grade fPPG waveforms to improve the extraction of cardiovascular features. For clinical evaluation, we use the corresponding ECG signals as the reference. We extract R-peaks from the ECG signals based on the trained model by Gabbouj (2022). Pulse-pulse interval (PPI) is measured based on systolic/diastolic peaks extracted from both wPPG and fPPG using the peak detection techniques utilized in previous studies (Mahmud, 2022; Mahmud, 2023). When we correlate the HR and HRV extracted from the ground truth ECG signals with the PR and PRV from the PPG signals using the Pearson Correlation Coefficient (PCC) formulated in Eq. (23), we obtain the results presented in Table 2. The correlation between HRV and PRV is determined by using the SDNN metric formulated in Eq. (31). This choice is made because SDNN is considered a more robust measure of HRV than RMSSD, as it is utilized in state-of-the-art wearables like the Apple Watch (Kar, 2023).

The PCC between the PRs estimated from fPPG' generated by the **TTR-GAN** and the HRs extracted from the ground truth ECG signals improved by approximately **10.35 %** compared to PRs from the unrestored wPPG signals, increasing from 0.7968 to 0.9003 by dint of Translation Through Restoration. Before this, we observed an approximate 3.36 % (improved from 0.7968 to 0.8304) boost in the PCC between the HRs from the ECG and the PRs from the wPPG after restoration. On the other hand, when correlating HRV from ECG and PRV from fPPG' measured through SDNN, the **TTR-GAN** achieved an improvement of approximately **14.66 %**, increasing from 0.6991 to 0.8457 thanks to the Translation Through Restoration on the raw wPPG waveforms. Prior to this, we observed an approximate 4.47 % (improved from 0.6991 to 0.7438) boost in the PCC between the HRV from the ECGs and the PRV from the restored wPPGs.

To ensure that the extracted heart (or pulse) rate and variability ranges align with subject metadata and real-world trends, we examined four key metrics: mean HR/PR (in BPM), mean RR (in ms), mean HRV/PRV in terms of SDNN (ms) and RMSSD (ms) measured across the entire dataset. These results are presented in Table 3 where we can observe that the mean HRV (or PRV) values across different modalities are not as pronounced i.e., closely related as those for HRs (or PRs). However, **TTR-GAN** generated fPPG' signals closely approximate the ground truth fPPGs across all metrics. In general, the PPG waveforms exhibit a similar range of mean PRVs as the HRV from the ECG signals, even though the clinical parameters were extracted using different techniques. Furthermore, the extracted HR (or PR), RR, and HRV (or PRV) parameters align with the clinical range for healthy young subjects (Shaffer & Ginsberg, 2017; Aeschbacher, 2016), which make up the MAUS dataset. This alignment underscores the reliability of the analytical procedures employed in this section.

The trends in HR/PR and HRV/PRV across the entire dataset may not be readily apparent from the mean results presented in Table 3. Therefore, in Fig. 6 (a-d), we have plotted the HR, RRI, and HRV (RMSSD and SDNN) trends of ECG against PR, PPI, and PRV (RMSSD and SDNN) from wPPG, fPPG, and fPPG', respectively, with annotations for each subject. It is evident from these plots that **TTR-GAN** enhanced PR, PPI, and PRV performance for all subjects through restoration and translation, subject 14 being the most anomalous. However, the performance of fPPG' never surpasses that of fPPG in matching ECG, as fPPG serves as the ground truth for the **TTR-GAN**, and ECG has been used solely for clinical evaluation. Scatter plots in Fig. 6 (e, f) illustrate the correlations between PRs extracted from fPPG and wPPG, and from fPPG and fPPG', respectively. We can conclude that **TTR-GAN** has improved the correlation,

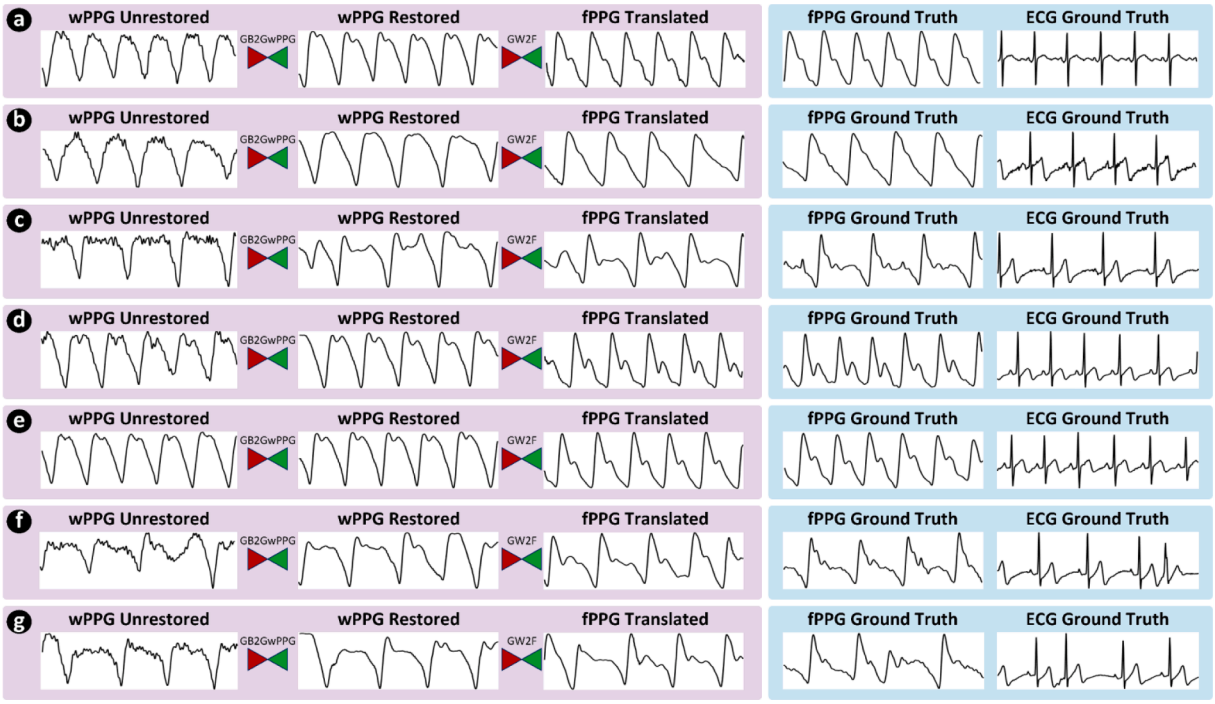

Fig. 8. Qualitative visualization of outcomes from different stages of the proposed **TTR-GAN** framework: **(a)-(e)** for healthy cases and **(f)-(g)** for unhealthy cases.

particularly by rectifying some highly erroneous samples (i.e., outliers) through efficient wPPG restoration and fPPG' synthesis.

3.4. Qualitative evaluation

In this section, we conduct a qualitative evaluation of the wPPG restoration and w2fPPG translation schemes of the proposed **TTR-GAN** framework through effective visualizations.

3.4.1. Blind wrist PPG restoration

In the blind wPPG restoration scheme, our goal is to restore or clean the wPPG signals, regardless of their quality or the type of artifact. In Fig. 7, we showcase corresponding wPPG, wVPG, and wAPG signals of varying quality and morphology before and after restoration, along with the ApEn measurements for wPPG. From all the provided samples, it is evident that CycleGAN restored the signals without affecting their morphology. In Fig. 7 (a) and Fig. 7 (b), wPPG and its derivatives were restored from high-frequency distortions that cannot be cleaned through traditional signal processing techniques (e.g., filtration). In a resting condition, wearable wristwatches (the primary data acquisition device for this study) exhibit more consistent skin contact pressure compared to clip-based clinical fPPG recording systems. However, as wearables are used during daily activities, skin contact may vary due to sudden movements. Fig. 7 (c) illustrates a unique scenario where CycleGAN restored a segment that was distorted as a result of fluctuations in skin contact pressure. Lastly, Fig. 7 (d) represents a case where the input wPPG signal is of high quality. The signal was almost untouched by the system, thus demonstrating its robustness. Tsai et al. (Tsai, 2021), in their study, inserted back lost features to manually restore distorted PPG signals, which is being efficiently performed here by 1D-CycleGANs on a much more diverse dataset.

3.4.2. Wrist-to-finger PPG synthesis

The wrist-to-finger PPG signal synthesis performance of the translator CycleGAN improved after wPPG restoration, as discussed in the quantitative analysis section. Fig. 8 displays some sample intermediate and final outputs from the **TTR-GAN** framework (3-channel approach) for qualitative evaluation. It is evident that the translated fPPG waveforms closely resemble the ground truth fPPG signals, regardless of the quality of the input wPPGs, thanks to the restoration. This also demonstrates that CycleGAN can effectively translate fPPG waveforms irrespective of the morphology of the input wPPG signals. Although the MAUS dataset was collected from healthy volunteers, as per the dataset description, for one subject (subject 14), the presence of heart arrhythmia could be observed. As shown in Fig. 8 (f, g), these segments exhibit high HRV/PRV, as reflected in the ECG, fPPG, and wPPG waveforms. These signals posed a challenge for the CycleGAN to accurately regenerate, primarily due to their rarity in the dataset (also

Table 4
Computational costs, model parameters, and TTR-GAN (3-channel) performance in restoration and synthesis across different types of neural networks.

Neural Network Type	Restoration Model Architecture	PRTX Performance (%)	Total Parameters (M)	Inference Time (ms)	Translation Model Architecture	Performance (%)		Total Parameters (M)	Inference Time (ms)
						HR	HRV		
CNN	ResNet-9blocks	32.8	0.240	12.9	UNet	9.6	12.6	0.853	6.61
Self-ONN (q[a] = 3)		33.7	0.715	18.2		9.8	12.9	2.176	15.7
Super-ONN (q = 3, sf[b]=2)		35.9	1.048	26.7		10.4	14.7	2.184	23.0

a. q: Polynomial Order.
b. sf: Kernel Shifting.

reflected in Fig. 6). Nevertheless, this opens up the possibility of employing 1D-CycleGANs to correctly detect cardiovascular anomalies from wPPG signals collected from wearables, provided that such data is abundant in the training set.

3.5. Computational cost and portability of TTR-GAN

Considering that the primary application of the proposed **TTR-GAN** framework is in wearable devices, such as wristwatches, the models need to be lightweight to accommodate the memory and processing limitations inherent in these devices. While the training process of CycleGANs can be computationally expensive, the testing setup can be considerably simpler. As illustrated in Fig. 1, a typical implementation of the proposed three-channel **TTR-GAN** involves four trained generators: three for wPPG, wVPG, and wAPG restoration (*GB2GwPPG, GB2GwVPG, GB2GwAPG*), and one for multichannel w2fPPG translation (*GW2F*). Two primary factors influencing the computational cost of deep learning models are their complexity and the total number of parameters (Hu, Chu, Pei, Liu, & Bian, 2021). As part of an ablation study, we implemented the CycleGAN generators for both restoration and translation phases using CNN, Self-ONN, and Super-ONN, while keeping the discriminators the same. Table 4 provides their overall performance metrics and computational costs.

In Table 4, we present the computational cost in two ways: total model parameters and inference time. Model inference time is a metric influenced by both model complexity and the total number of parameters (Hu et al., 2021). Therefore, instead of relying on a vague term like "model complexity," we utilize inference time, which encompasses all relevant factors. The influence of model complexity on inference time is evident from the ResNet-9block generators. Despite being much lighter than the UNet-structured models, they are computationally more expensive due to the residual layers in the bottleneck, which significantly increases their inference time. On the other hand, based on Table 4, Super-ONN, as expected, is more computationally demanding than its CNN and Self-ONN counterparts, despite having the same model architecture and hyperparameters. Nevertheless, Super-ONN also exhibits slightly better performance than them. In real-life applications, engineers need to carefully consider the tradeoff between computational and memory requirements and performance improvements when choosing the appropriate framework for their devices. Regarding memory requirements for Super-ONN-based models, the ResNet-9blocks-based trained generator for wPPG restoration contains approximately 1.048 million (M) parameters, while the UNet-based trained generator for w2fPPG translation comprises about 2.184 M parameters. In total, these parameters sum up to roughly 6.044 M parameters for the three-channel approach, which equates to around 6 megabytes (MB) of device memory. This requirement can be easily accommodated by most contemporary wearable devices (Sabry, Eltaras, Labda, Alzoubi, & Malluhi, 2022).

3.6. Comparison to existing literature

As detailed in the methodology, **TTR-GAN** is capable of restoring and translating signals solely through the use of 1D-CycleGANs. It is not equipped to directly estimate heart rates from PPG signals, necessitating the use of external tools. Existing literature contains various studies on heart rate extraction from wPPG signals, many of which have been evaluated on benchmark datasets. Some studies have focused on machine learning-based algorithms, as mentioned in the introduction. However, based on our comprehensive literature review, we have found no study comparable to **TTR-GAN**, which employs a cascading approach of 1D-CycleGANs and harnesses their restoration and translation capabilities to enhance a corrupted PPG dataset and its clinical relevance. Prior studies, such as: (Kiranyaz et al.; Mehrabadi et al., 2022; Aqajari, Cao, Zargari, & Rahmani, 2021), have employed 1D-CycleGANs for specific applications like blind ECG restoration, PPG to Arterial Blood Pressure (ABP) synthesis, Respiratory Rate translation, etc. Therefore, given the novelty of our approach within the field of signal processing, direct comparison with existing literature is not feasible.

3.7. Study limitations and future directions for research

The proposed **TTR-GAN** comprises two cascaded sub-frameworks for restoration and synthesis, respectively. Future studies could investigate the combination of these two frameworks to conduct restoration and synthesis of wPPG signals through a single CycleGAN or similar deep learning frameworks. This enhancement would simplify and make the framework more portable, making it well-suited for wearable devices. As a suggestion, this can be achieved by utilizing fPPG waveforms as the target for the unpaired restoration scheme in **TTR-GAN**, instead of using clean wPPG. **TTR-GAN**, in its current form, exclusively operates on data from healthy volunteers, as available in the MAUS dataset (Beh & Wu, 2022; Beh et al., 2021). Incorporating data from unhealthy patients would introduce an additional layer of challenge for researchers, as they would need to restore the waveforms without affecting the various cardiac anomalies present. Future studies can explore similar frameworks with unhealthy data and attempt to enhance cardiac anomaly detection and/or classification from real-time wPPG signals.

4. Conclusion

In conclusion, modern wearable devices often employ wrist PPG signals to estimate vital cardiovascular parameters, such as heart rate, which are significantly affected by motion. In this study, we introduce **TTR-GAN**, a framework that blindly restores corrupted wrist PPG signals and translates them into finger PPG waveforms using 1D-CycleGANs, thereby yielding accurate pulse-pulse interval and pulse rate variation readings. The blindly restored wrist PPG signals exhibited significantly lower entropy than the corrupted input samples, demonstrating the platform's artifact removal capability. Utilizing the proposed **PRTX** metric, which is insensitive to phase shifts between wrist and finger PPG signals, we observed both temporal and spectral correlation between the translated finger PPG and the ground truth finger PPG and reached an overall improvement of **35.88 %** through **TTR-GAN**. Furthermore, the correlation between pulse rate and pulse rate variability of the **TTR-GAN** generated fPPG signals, in comparison to the heart rate and heart rate variations extracted from ground truth ECG signals, improved by approximately **10.4 %** and **14.7 %**, respectively, when contrasted with the raw wrist PPG signals. **TTR-GAN**, due to its computational efficiency, can be readily integrated into wearable devices that collect wrist PPG signals, providing improved real-time cardiovascular monitoring and enhancing clinical decision-making. In future research, the combination of the restoration and translation schemes of **TTR-GAN** into a single unified framework can be explored to enhance portability and simplicity for wearables. Researchers in this field may also delve into similar frameworks with unhealthy data, aiming to enhance cardiac anomaly detection and/or classification from real-time wPPG signals.

Funding

This work was supported in part by the Qatar National Research Fund under Grant NPRP12S-0227–190164 and is also supported via funding from Prince Sattam Bin Abdulaziz University project number (PSAU/2023/R/1444). The statements made herein are solely the responsibility of the authors. The open-access publication is supported by the Qatar National Library.

CRediT authorship contribution statement

Sakib Mahmud: Conceptualization, Methodology, Software, Writing – original draft, Writing – review & editing. **Muhammad E.H.**

Chowdhury: Conceptualization, Methodology, Supervision, Funding acquisition, Writing – original draft, Writing – review & editing. **Serkan Kiranyaz:** Methodology, Validation, Software, Writing – review & editing. **Malisha Islam Tapotee:** Conceptualization, Methodology, Validation, Software, Writing – original draft. **Purnata Saha:** . **Anas M. Tahir:** Methodology, Validation, Software. **Amith Khandakar:** Validation, Supervision, Funding acquisition, Writing – review & editing. **Abdulrahman Alqahtani:** Validation, Supervision, Writing – original draft, Writing – review & editing.

Declaration of competing interest

The authors declare that they have no known competing financial interests or personal relationships that could have appeared to influence the work reported in this paper.

Data availability

The preprocessed data set will be made available on reasonable request to the corresponding author.

Appendix A. Supplementary data

Supplementary data to this article can be found online at https://doi.org/10.1016/j.eswa.2024.123167.

References

Aeschbacher, S., et al. (2016). Healthy lifestyle and heart rate variability in young adults. *European Journal of Preventive Cardiology, 23*(10), 1037–1044. https://doi.org/10.1177/2047487315623708

Ahishali, M., Degerli, A., Kiranyaz, S., Hamid, T., Mazhar, R., & Gabbouj, M. R2C-GAN: Restore-to-classify GANs for blind X-ray restoration and COVID-19 classification, arXiv [eess.IV], 2022. [Online]. Available: 10.48550/arXiv.2209.14770.

Albuquerque, I., et al. (2020). WAUC: A multi-modal database for mental workload assessment under physical activity. *Frontiers in Neuroscience, 14*. https://doi.org/10.3389/fnins.2020.549524

Alonzo, L. M. B., & Co, H. S. Ensemble Empirical Mode Decomposition of Photoplethysmogram Signals for Assessment of Ventricular Fibrillation," 2018 IEEE 10th International Conference on Humanoid, Nanotechnology, Information Technology, Communication and Control, Environment, and Management (HNICEM), 2018, pp. 1-4, doi: 10.1109/HNICEM.2018.8666241.

Aqajari, S. A. H., Cao, R., Zargari, A. H. A., & Rahmani, A. M. An end-to-end and accurate ppg-based respiratory rate estimation approach using cycle generative adversarial networks, 2021 43rd Annual International Conference of the IEEE Engineering in Medicine & Biology Society (EMBC), Mexico, 2021, pp. 744-747, doi: 10.1109/EMBC46164.2021.9629984.

Armanious, K., Jiang, C., Abdulatif, S., Küstner, T., Gatidis, S., & Yang, B. Unsupervised medical image translation using cycle-MedGAN, 2019 27th European Signal Processing Conference (EUSIPCO), A Coruna, Spain, 2019, pp. 1-5, doi: 10.23919/EUSIPCO.2019.8902799.

Bailey, J., et al. (1990). Recommendations for standardization and specifications in automated electrocardiography: Bandwidth and digital signal processing. A report for health professionals by an ad hoc writing group of the Committee on Electrocardiography and Cardiac Electrophysiology of the Council on Clinical Cardiology, American Heart Association. *Circulation, 81*(2), 730–739. https://doi.org/10.1161/01.cir.81.2.730

Bandt, C., & Pompe, B. Permutation entropy: A natural complexity measure for time series, Physical Review Letters, vol. 88, no. 17, 2002, doi: 10.1103/PhysRevLett.88.174102.

Banik, P., Hossain, S., Kwon, T., Kim, H., & Kim, K. (2020). Development of a wearable reflection-type pulse oximeter system to acquire clean PPG signals and measure pulse rate and SpO2 with and without finger motion. *Electronics, 9*(11), 1905. https://doi.org/10.3390/electronics9111905

Basak, P., et al. (2024). A novel deep learning technique for morphology preserved fetal ECG extraction from mother ECG using 1D-CycleGAN. *Expert Systems with Applications, 235*(121196), Article 121196. https://doi.org/10.1016/j.eswa.2023.121196

Beh, W., & Wu, Y. MAUS: A Dataset for Mental Workload Assessment on N-back Task Using Wearable Sensor, arXiv.org, 2022. [Online]. Available: https://doi.org/10.48550/arXiv.2111.02561. (accessed Oct 05, 2022).

Beh, W.-K., & Yi-Hsuan, W.u. (2021). MAUS: A dataset for mental workload assessment on N-back task using wearable sensor. *IEEE Dataport*. https://doi.org/10.21227/q4td-yd35

Bio-medical.com, 2022. [Online]. Available: https://bio-medical.com/media/support/sa7510.pdf. (accessed Oct 05, 2022).

Biswas, D., et al. (2019). CorNET: Deep learning framework for PPG-based heart rate estimation and biometric identification in ambulant environment. *IEEE Transactions on Biomedical Circuits and Systems, 13*(2), 282–291. https://doi.org/10.1109/tbcas.2019.2892297

Bracewell, R. N. (1999). *The Fourier transform and its applications*. Boston, MA: McGraw-Hill.

Burrello, A., et al. (2021). Q-PPG: Energy-efficient PPG-based heart rate monitoring on wearable devices. *IEEE Transactions on Biomedical Circuits and Systems, 15*(6), 1196–1209. https://doi.org/10.1109/tbcas.2021.3122017

Cacciatori, V., et al. (1996). Power spectral analysis of heart rate in hyperthyroidism. *The Journal of Clinical Endocrinology and Metabolism, 81*(8), 2828–2835. https://doi.org/10.1210/jcem.81.8.8768838

Cai, Z., et al. (2020). An open-access long-term wearable ECG database for premature ventricular contractions and supraventricular premature beat detection. *J. Med. Imaging Health Inform., 10*(11), 2663–2667. https://doi.org/10.1166/jmihi.2020.32892663

Chan, G., et al. (2019). Multi-site photoplethysmography technology for blood pressure assessment: Challenges and recommendations. *Journal of Clinical Medicine, 8*(11), 1827. https://doi.org/10.3390/jcm8111827

Chen, W., Wang, Z., Xie, H., & Yu, W. (June 2007). Characterization of surface EMG Signal based on fuzzy entropy. *IEEE Transactions on Neural Systems and Rehabilitation Engineering, 15*(2), 266–272. https://doi.org/10.1109/TNSRE.2007.897025

Chowdhury, S., Hyder, R., Hafiz, M., & Haque, M. (2018). Real-time robust heart rate estimation from wrist-type PPG signals using multiple reference adaptive noise cancellation. *IEEE Journal of Biomedical and Health Informatics, 22*(2), 450–459. https://doi.org/10.1109/jbhi.2016.2632201

Chowdhury, M. H., et al. (2020). Estimating blood pressure from the photoplethysmogram signal and demographic features using Machine Learning Techniques. *Sensors, 20*(11), 3127. https://doi.org/10.3390/s20113127

Chowdhury, M. H., et al. (2022). Lightweight end-to-end deep learning solution for estimating the respiration rate from Photoplethysmogram signal. *Bioengineering, 9*(10), 558. https://doi.org/10.3390/bioengineering9100558

Cross-correlation. (2022). Cross-Correlation. Online accessed Nov 05 *Available* https://mathworld.wolfram.com/Cross-Correlation.html.

Dai, L., & Tang, J. iFlowGAN: An invertible flow-based generative adversarial network for unsupervised image-to-image translation, in IEEE Transactions on Pattern Analysis and Machine Intelligence, vol. 44, no. 8, pp. 4151-4162, 1 Aug. 2022, doi: 10.1109/TPAMI.2021.3062849.

Ewing, D. (1981). Heart rate changes in diabetes mellitus. *Lancet, 317*(8213), 183–186. https://doi.org/10.1016/S0140-6736(81)90061-1

Fujita, Y., Hiromoto, M., & Sato, T. (2018). PARHELIA: Particle filter-based heart rate estimation from photoplethysmographic signals during physical exercise. *IEEE Transactions on Biomedical Engineering, 65*(1), 189–198. https://doi.org/10.1109/tbme.2017.2697911

Gabbouj, M. et al., Robust peak detection for Holter ECGs by self-organized operational neural networks, IEEE Trans. Neural Netw. Learn. Syst., vol. PP, 2022, doi: 10.1109/TNNLS.2022.3158867.

Gjoreski, M., et al. (2020). Datasets for cognitive load inference using wearable sensors and psychological traits. *Applied Sciences, 10*(11), 3843. https://doi.org/10.3390/app10113843

Golap, M., Raju, S., Haque, M., & Hashem, M. (2021). Hemoglobin and glucose level estimation from PPG characteristics features of fingertip video using MGGP-based model. *Biomedical Signal Processing and Control, 67*, Article 102478. https://doi.org/10.1016/j.bspc.2021.102478

Goodfellow, I. J. et al., Generative adversarial networks, arXiv.org, 2014. [Online]. Available: 10.48550/arXiv.1406.2661.

Gorman, J. M., & Sloan, R. P. (2000). Heart rate variability in depressive and anxiety disorders. *American Heart Journal, 140*(4), S77–S83. https://doi.org/10.1067/mhj.2000.109981

Han, D., et al. (2020). Premature atrial and ventricular contraction detection using photoplethysmographic data from a smartwatch. *Sensors, 20*(19), 5683. https://doi.org/10.3390/s20195683

Hartmann, V., Liu, H., Chen, F., Hong, W., Hughes, S., & Zheng, D. (2019). Toward accurate extraction of respiratory frequency from the photoplethysmogram: Effect of measurement site. *Frontiers in Physiology, 10*. https://doi.org/10.3389/fphys.2019.00732

Hartmann, V., Liu, H., Chen, F., Qiu, Q., Hughes, S., & Zheng, D. (2019). Quantitative comparison of photoplethysmographic waveform characteristics: effect of measurement site. *Frontiers in Physiology, 10*. https://doi.org/10.3389/fphys.2019.00198

Hartmann, K., Schirrmeister, R., & Ball, T. EEG-GAN: Generative adversarial networks for electroencephalographic (EEG) brain signals, arXiv.org, 2022. [Online]. Available: 10.48550/arXiv.1806.01875. (accessed Sep 03, 2022).

Hasty, F., García, G., Dávila, H., Wittels, S. H., Hendricks, S., & Chong, S. Heart rate variability as a possible predictive marker for the acute inflammatory response in COVID-19 patients, Military Medicine, vol. 186, no. 1-2, 2021, doi: 10.1093/milmed/usaa405.

Herrmann, B., et al. (2020). Central hypothyroidism impairs heart rate stability and prevents thyroid hormone-induced cardiac hypertrophy and pyrexia. *Thyroid, 30*(8), 1205–1216. https://doi.org/10.1089/thy.2019.0705

Hu, X., Chu, L., Pei, J., Liu, W., & Bian, J. (2021). Model complexity of deep learning: A survey. *Knowledge and Information Systems, 63*(10), 2585–2619. https://doi.org/10.1007/s10115-021-01605-0

Huang, H. et al., UNet 3+: A full-scale connected unet for medical image segmentation, arXiv.org, 19-Apr-2020. [Online]. Available: 10.48550/arXiv.2004.08790. (accessed Nov 08, 2022).

Ibtehaz, N., et al. (2022). PPG2ABP: Translating photoplethysmogram (PPG) signals to arterial blood pressure (ABP) waveforms. *Bioengineering, 9*(11), 692. https://doi.org/10.3390/bioengineering9110692

Ismail, S., Siddiqi, I., & Akram, U. (2022). Heart rate estimation in PPG signals using convolutional-recurrent regressor. *Computers in Biology and Medicine, 145*, Article 105470. https://doi.org/10.1016/j.compbiomed.2022.105470

Isola, P., Zhu, J.-Y., Zhou, T., & Efros, A. A. Image-to-image translation with conditional adversarial networks, arXiv.org, 26-Nov-2018. [Online]. Available: 10.48550/arXiv.1611.07004. (accessed Nov 08, 2022).

Jarchi, D., & Casson, A. (2017). Towards photoplethysmography-based estimation of instantaneous heart rate during physical activity. *IEEE Transactions on Biomedical Engineering, 64*(9), 2042–2053. https://doi.org/10.1109/tbme.2017.2668763

Jia, P., Huang, Y., Cai, B., & Cai, D. (2019). Solar image restoration with the CycleGAN based on multi-fractal properties of texture features. *The Astrophysical Journal, 881*(2), L30. https://doi.org/10.3847/2041-8213/ab365f

Jiao, Y., Deng, Y., Luo, Y., & Lu, B. (2020). Driver sleepiness detection from EEG and EOG signals using GAN and LSTM networks. *Neurocomputing, 408*, 100–111. https://doi.org/10.1016/j.neucom.2019.05.108

Johnson, A. et al., MIMIC-III, a freely accessible critical care database, Scientific Data, vol. 3, no. 1, 2016, doi: 10.1038/sdata.2016.35.

Jönsson, B., Laurent, C., Eneling, M., Skau, T., & Lindberg, L. (2005). Automatic ankle pressure measurements using PPG in ankle-brachial pressure index determination. *European Journal of Vascular and Endovascular Surgery, 30*(4), 395–401. https://doi.org/10.1016/j.ejvs.2005.05.012

Kanti Podder, K., et al. (2023). Deep learning-based middle cerebral artery blood flow abnormality detection using flow velocity waveform derived from transcranial Doppler ultrasound. *Biomedical Signal Processing and Control, 85*, Article 104882. https://doi.org/10.1016/j.bspc.2023.104882

Kar, S. N. Apple Watch guide to understanding and using HRV (Heart Rate Variability), MyHealthyApple, 05-Oct-2020. [Online]. Available: https://www.myhealthyapple.com/guide-to-understanding-and-using-heart-rate-variability-hrv-on-your-apple-watch/. (accessed Sep 24, 2023).

Karras, T., Laine, S. & Aila, T. A style-based generator architecture for generative adversarial networks, in IEEE Transactions on Pattern Analysis and Machine Intelligence, vol. 43, no. 12, pp. 4217-4228, 1 Dec. 2021, doi: 10.1109/TPAMI.2020.2970919.

Kim, T., Cha, M., Kim, H., Lee, J. K., & Kim, J. Learning to discover cross-domain relations with generative adversarial networks, arXiv.org, 2017. [Online]. Available: 10.48550/arXiv.1703.05192.

Kiranyaz, S. et al., Super Neurons, in IEEE Transactions on Emerging Topics in Computational Intelligence, doi: 10.1109/TETCI.2023.3314658.

Kiranyaz, S., Ince, T., Iosifidis, A., & Gabbouj, M. (2020). Operational neural networks. *Neural Computing and Applications, 32*(11), 6645–6668. https://doi.org/10.1007/s00521-020-04780-3

Kiranyaz, S., Malik, J., Abdallah, H. B., Ince, T., Iosifidis, A., Gabbouj, M. Self-organized operational neural networks with generative neurons, Neural Networks (Elsevier), pp. 140:294-308, Aug. 2021, doi: 10.1016/j.neunet.2021.02.028.

Kiranyaz, S., Malik, J., Gabbouj, M. & Ince, T. Operational Neural Networks, Selfonn.net, 2022. [Online]. Available: http://selfonn.net/. (accessed Oct 01, 2022).

Kiranyaz, S. et al., Blind ECG restoration by operational cycle-GANs, in IEEE Transactions on Biomedical Engineering, doi: 10.1109/TBME.2022.3172125.

Lan, K.-C., Raknim, P., Kao, W.-F., & Huang, J.-H. Toward hypertension prediction based on PPG-derived HRV signals: A feasibility study, Journal of Medical Systems, vol. 42, no. 6, 2018, doi: 10.1007/s10916-018-0942-5.

Lata, K., Dave, M., & Nishanth, K. N. Image-to-image translation using generative adversarial network, 2019 3rd International conference on Electronics, Communication and Aerospace Technology (ICECA), Coimbatore, India, 2019, pp. 186-189, doi: 10.1109/ICECA.2019.8822195.

Lee, H., Chung, H., & Lee, J. (2019). Motion artifact cancellation in wearable photoplethysmography using gyroscope. *IEEE Sensors Journal, 19*(3), 1166–1175. https://doi.org/10.1109/jsen.2018.2879970

Lelovas, P., Dontas, I., Bassiakou, E., & Xanthos, T. (2008). Cardiac implications of Lyme disease, diagnosis and therapeutic approach. *International Journal of Cardiology, 129*(1), 15–21. https://doi.org/10.1016/j.ijcard.2008.01.044

Li, Z., Liu, F., Yang, W., Peng, S., & Zhou, J. A survey of convolutional neural networks: analysis, applications, and prospects, in IEEE Transactions on Neural Networks and Learning Systems, doi: 10.1109/TNNLS.2021.3084827.

Li, Y., Tang, S., Zhang, R., Zhang, Y., Li, J., & Yan, S. (Dec. 2019). Asymmetric GAN for unpaired image-to-image translation. *IEEE Transactions on Image Processing, 28*(12), 5881–5896. https://doi.org/10.1109/TIP.2019.2922854

Lin, G., Zhang, J., & Liu, Y. Single shot reversible GAN for BCG artifact removal in simultaneous EEG-fMRI, arXiv.org, 2022. [Online]. Available: 10.48550/arXiv.2011.01710. (accessed Sep 03, 2022).

Liu, W., Fang, X., Chen, Q., Li, Y., & Li, T. (2018). Reliability analysis of an integrated device of ECG, PPG, and pressure pulse wave for cardiovascular disease. *Microelectronics Reliability, 87*, 183–187. https://doi.org/10.1016/j.microrel.2018.06.008

Long, N., Kim, J., Lee, B. & Chung, W. CycleGAN based motion artifact cancellation for photoplethysmography wearable device, Intelligent Human Computer Interaction, pp. 138-144, 2022, doi: 10.1007/978-3-030-98404-5_13.

Luo, Y., & Lu, B.-L. (2018). EEG Data Augmentation for Emotion Recognition Using a Conditional Wasserstein GAN. In *2018 40th Annual International Conference of the IEEE Engineering in Medicine and Biology Society (EMBC)* (pp. 2535–2538). https://doi.org/10.1109/EMBC.2018.8512865

Mahmud, S., Chowdhury, M. E. H., Kiranyaz, S., Al Emadi, N., Tahir, A. M., Hossain, M. S., … Al-Maadeed, S. (2024). Restoration of motion-corrupted EEG signals using attention-guided operational CycleGAN. *Engineering Applications of Artificial Intelligence, 128*(107514), 107514. https://doi.org/10.1016/j.engappai.2023.107514

Mahmud, S., et al. (2022). A shallow U-net architecture for reliably predicting blood pressure (BP) from photoplethysmogram (PPG) and electrocardiogram (ECG) signals. *Sensors, 22*(3), 919. https://doi.org/10.3390/s22030919

Mahmud, S., et al. (2023). NABNet: A nested attention-guided BICONVLSTM network for a robust prediction of blood pressure components from reconstructed arterial blood pressure waveforms using PPG and ECG signals. *Biomedical Signal Processing and Control, 79*, Article 104247. https://doi.org/10.1016/j.bspc.2022.104247

Malik, J., Devecioglu, O. C., Kiranyaz, S., Ince, T. & Gabbouj, M., Real-time patient-specific ECG classification by 1D self-operational neural networks, in IEEE Transactions on Biomedical Engineering, doi: 10.1109/TBME.2021.3135622.

Malik, J., Kiranyaz, S., & Gabbouj, M. (2021). Self-organized operational neural networks for severe image restoration problems. *Neural Networks (Elsevier), 135*, 201–211. https://doi.org/10.1016/j.neunet.2020.12.014

Mao, X., Li, Q., Xie, H., Lau, R. Y. K., Wang, Z. & Smolley, S. P. Least squares generative adversarial networks, 2017 IEEE International Conference on Computer Vision (ICCV), Venice, Italy, 2017, pp. 2813-2821, doi: 10.1109/ICCV.2017.304.

Markova, V., Ganchev, T., & Kalinkov, K. (2019). CLAS: A database for cognitive load, affect and stress recognition. In *in 2019 International Conference on Biomedical Innovations and Applications (BIA). IEEE* (pp. 1–4). https://doi.org/10.1109/BIA48344.2019.8967457

Martínez, G., Howard, N., Abbott, D., Lim, K., Ward, R., & Elgendi, M. Can Photoplethysmography replace arterial blood pressure in the assessment of blood pressure?, 2022, doi: 10.3390/jcm7100316.

Marzorati, D., Bovio, D., Salito, C., Mainardi, L., & Cerveri, P. (2020). Chest wearable apparatus for cuffless continuous blood pressure measurements based on PPG and PCG signals. *IEEE Access, 8*, 55424–55437. https://doi.org/10.1109/ACCESS.2020.2981300

Mason, K. P., & Lönnqvist, P.-A. (2015). Bradycardia in perspective—not all reductions in heart rate need immediate intervention. *Paediatric Anaesthesia, 25*(1), 44–51. https://doi.org/10.1111/pan.12584

Mehrabadi, M. A., Aqajari, S. A. H., Zargari, A. H. A., Dutt, N., & Rahmani, A. M. Novel blood pressure waveform reconstruction from photoplethysmography using cycle generative adversarial networks, 2022 44th Annual International Conference of the IEEE Engineering in Medicine & Biology Society (EMBC), Glasgow, Scotland, United Kingdom, 2022, pp. 1906-1909, doi: 10.1109/EMBC48229.2022.9871962.

Mijić, I., Šarlija, M., & Petrinović, D. MMOD-COG: A database for multimodal cognitive load classification, 2019 11th International Symposium on Image and Signal Processing and Analysis (ISPA), Dubrovnik, Croatia, 2019, pp. 15-20, doi: 10.1109/ISPA.2019.8868678.

"MIMIC-III Waveform Database v1.0", Doi.org, 2022. [Online]. Available: https://doi.org/10.13026/c2607m. (accessed Sep 02, 2022).

Mohebbian, M. R., Vedaei, S. S., Wahid, K. A., Dinh, A., Marateb, H. R., & Tavakolian, K. (Feb. 2022). Fetal ECG extraction from maternal ECG using attention-based CycleGAN. *IEEE Journal of Biomedical and Health Informatics, 26*(2), 515–526. https://doi.org/10.1109/JBHI.2021.3111873

Monge-Álvarez, J. A set of entropy measures for temporal series (1D signals), MathWorks, 01-Nov-2022. [Online]. Available: https://www.mathworks.com/matlabcentral/fileexchange/50289-a-set-of-entropy-measures-for-temporal-series-1d-signals?s_tid=mwa_osa_a. (accessed Nov 02, 2022).

Mostofa, M., Ferdous, S. N., Riggan, B. S., & Nasrabadi, N. M. (2020). Joint-SRVDNet: Joint super resolution and vehicle detection network. *IEEE Access, 8*, 82306–82319. https://doi.org/10.1109/ACCESS.2020.2990870

Nardelli, M., Vanello, N., Galperti, G., Greco, A., & Scilingo, E. (2020). Assessing the quality of heart rate variability estimated from wrist and finger PPG: A novel approach based on cross-mapping method. *Sensors, 20*(11), 3156. https://doi.org/10.3390/s20113156

Olshansky, B., Ricci, F., & Fedorowski, A. (2022). Importance of resting heart rate. *Trends in Cardiovascular Medicine*. https://doi.org/10.1016/j.tcm.2022.05.006

Paliakaitė, B., et al. (2021). Blood pressure estimation based on photoplethysmography: Finger versus wrist. *Computing in Cardiology (CinC), 2021*, 1–4. https://doi.org/10.23919/CinC53138.2021.9662716

Panwar, M., Gautam, A., Biswas, D., & Acharyya, A. (2020). PP-Net: A deep learning framework for PPG-based blood pressure and heart rate estimation. *IEEE Sensors Journal, 20*(17), 10000–10011. https://doi.org/10.1109/jsen.2020.2990864

Papoulis, A. (1994). *The Fourier integral, and its applications*. New York: McGraw-Hill.

"Peak analysis," Mathworks.com. [Online]. Available: https://www.mathworks.com/help/signal/ug/peak-analysis.html. (accessed Jun 30, 2023).

Peng, J., Wu, X., Yang, X., Huang, Y., Cai, B., & Cai, D. (2020). Astronomical image restoration and point spread function estimation with deep neural networks. *Advances in Optical Astronomical Instrumentation, 2019*. https://doi.org/10.1117/12.2541083

Perret-Guillaume, C., Joly, L., & Benetos, A. (2009). Heart rate as a risk factor for cardiovascular disease. *Progress in Cardiovascular Diseases, 52*(1), 6–10. https://doi.org/10.1016/j.pcad.2009.05.003

Pilt, K., Ferenets, R., Meigas, K., Lindberg, L., Temitski, K., & Viigimaa, M. (2013). New photoplethysmographic signal analysis algorithm for arterial stiffness estimation. *The Scientific World Journal, 2013*, 1–9. https://doi.org/10.1155/2013/169035

Pimentel, M. A. F., et al. (Aug. 2017). Toward a robust estimation of respiratory rate from pulse oximeters. *IEEE Transactions on Biomedical Engineering, 64*(8), 1914–1923. https://doi.org/10.1109/TBME.2016.2613124

Pincus, S. M., Gladstone, I. M., & Ehrenkranz, R. A. (1991). A regularity statistic for medical data analysis. *Journal of Clinical Monitoring, 7*(4), 335–345. https://doi.org/10.1007/BF01619355

"Plethysmography: Purpose, Procedure & Preparation", Healthline, 2022. [Online]. Available: https://www.healthline.com/health/plethysmography. (accessed Sep 01, 2022).
Porta, A., et al. (1998). Measuring regularity by means of a corrected conditional entropy in sympathetic outflow. *Biological Cybernetics, 78*(1), 71–78. https://doi.org/10.1007/s004220050414
Qiblawey, Y., et al. (2021). Detection and severity classification of COVID-19 in CT images using deep learning. *Diagnostics, 11*(5), 893. https://doi.org/10.3390/diagnostics11050893
Qin, Z., Li, M., Huang, L., & Zhao, Y. (2017). Stress level evaluation using BP Neural network based on time-frequency analysis of HRV. In *in 2017 IEEE International Conference on Mechatronics and Automation (ICMA)*. https://doi.org/10.1109/ICMA.2017.8016090
Radford, A., Metz, L., & Chintala, S. Unsupervised representation learning with deep convolutional generative adversarial networks, arXiv.org, 2015. [Online]. Available: 10.48550/arXiv.1511.06434.
Rajala, S., Lindholm, H., & Taipalus, T. (2018). Comparison of photoplethysmogram measured from wrist and finger and the effect of measurement location on pulse arrival time. *Physiological Measurement, 39*(7), Article 075010. https://doi.org/10.1088/1361-6579/aac7ac
Reiss, A., Indlekofer, I., Schmidt, P., & Van Laerhoven, K. (2019). Deep PPG: Large-scale heart rate estimation with convolutional neural networks. *Sensors, 19*(14), 3079. https://doi.org/10.3390/s19143079
Reşit Kavsaoğlu, A., Polat, K., & Recep Bozkurt, M. (2014). A novel feature ranking algorithm for biometric recognition with PPG signals. *Computers in Biology and Medicine, 49*, 1–14. https://doi.org/10.1016/j.compbiomed.2014.03.005
Richman, J. S., Moorman, J. R. Physiological time-series analysis using approximate entropy and sample entropy, American Journal of Physiology-Heart and Circulatory Physiology, vol. 278, no. 6, 2000, doi: 10.1152/ajpheart.2000.278.6.h2039.
Risso, M., et al. (2021). Robust and energy-efficient PPG-based heart-rate monitoring. *IEEE International Symposium on Circuits and Systems (ISCAS), 2021*, 1–5. https://doi.org/10.1109/ISCAS51556.2021.9401282
Rocha, L. G., et al. (Aug. 2020). Binary CorNET: Accelerator for HR estimation from wrist-PPG. *IEEE Transactions on Biomedical Circuits and Systems, 14*(4), 715–726. https://doi.org/10.1109/TBCAS.2020.3001675
Ronneberger, O., Fischer, P., & Brox, T. U-Net: convolutional networks for biomedical image segmentation, Lecture Notes in Computer Science, pp. 234–241, 2015, doi: 10.1007/978-3-319-24574-4_28.
Roy, B., & Gupta, R. (2020). MoDTRAP: Improved heart rate tracking and preprocessing of motion-corrupted photoplethysmographic data for personalized healthcare. *Biomedical Signal Processing and Control, 56*, Article 101676. https://doi.org/10.1016/j.bspc.2019.101676
Sabry, F., Eltaras, T., Labda, W., Alzoubi, K., & Malluhi, Q. (2022). Machine learning for healthcare wearable devices: The big picture. *Journal of Healthcare Engineering, 2022*, 1–25. https://doi.org/10.1155/2022/4653923
Sayem, F. R., Ahmed, M. U., Alam, S. B., Mahmud, S., Sheikh, M. M., Alqahtani, A., … Chowdhury, M. E. H. (2023). *A novel 1D generative adversarial network-based framework for atrial fibrillation detection using restored wrist photoplethysmography signals*. https://doi.org/10.48550/ARXIV.2312.09459.
Scardulla, F., D'Acquisto, L., Colombarini, R., Hu, S., Pasta, S., & Bellavia, D. A study on the effect of contact pressure during physical activity on photoplethysmographic heart rate measurements, 2022, doi: 10.3390/s20185052.
Schultz, J. C., Hilliard, A. A., Cooper, L. T., Jr, & Rihal, C. S. (2009). Diagnosis and treatment of viral myocarditis. *Mayo Clinic Proceedings, 84*(11), 1001–1009. https://doi.org/10.4065/84.11.1001
Seo, H., Yoon, G., Joo, S., & Nam, G. (2022). Multiple electrocardiogram generator with single-lead electrocardiogram. *Computer Methods and Programs in Biomedicine, 221*, Article 106858. https://doi.org/10.1016/j.cmpb.2022.106858
Shabaan, M., et al., Survey: smartphone-based assessment of cardiovascular diseases using ECG and PPG analysis, BMC Medical Informatics and Decision Making, vol. 20, no. 1, 2020, doi: 10.1186/s12911-020-01199-7.
Shaffer, F., & Ginsberg, J. P. An overview of heart rate variability metrics and norms, Front. Public Health, vol. 5, p. 258, 2017, doi: 10.3389%2Ffpubh.2017.00258.
Song, S., Nam, J., & Kim, J. (2021). NAS-PPG: PPG-based heart rate estimation using neural architecture search. *IEEE Sensors Journal, 21*(13), 14941–14949. https://doi.org/10.1109/jsen.2021.3073047
Spachos, P., Gao, J., & Hatzinakos, D. (2011). Feasibility study of photoplethysmographic signals for biometric identification. In *2011 17th International Conference on Digital Signal Processing (DSP)* (pp. 1–5). https://doi.org/10.1109/ICDSP.2011.6004938
Swai, J., Hu, Z., Zhao, X., Rugambwa, T., & Ming, G. Heart rate and heart rate variability comparison between postural orthostatic tachycardia syndrome versus healthy participants; a systematic review and meta-analysis, BMC Cardiovasc. Disord., vol. 19, no. 1, 2019, doi: 10.1186/s12872-019-01298-y.
Tahir, A. M., et al. (2021). Covid-19 infection localization and severity grading from chest X-ray images. *Computers in Biology and Medicine, 139*, Article 105002. https://doi.org/10.1016/j.compbiomed.2021.105002
Tang, H., Liu, H., Xu, D., Torr, P. H. S., & Sebe, N. AttentionGAN: unpaired image-to-image translation using attention-guided generative adversarial networks, in IEEE Transactions on Neural Networks and Learning Systems, doi: 10.1109/TNNLS.2021.3105725.
Tavakkoli, A., Kamran, S. A., Hossain, K. F., & Zuckerbrod, S. L. A novel deep learning conditional generative adversarial network for producing angiography images from retinal fundus photographs, Scientific Reports, vol. 10, no. 1, 2020, doi: 10.1038/s41598-020-78696-2.
Thomas, A., & Gopi, V. (2019). Accurate heart rate monitoring method during physical exercise from photoplethysmography signal. *IEEE Sensors Journal, 19*(6), 2298–2304. https://doi.org/10.1109/jsen.2018.2886001
Tsai, P., et al. (2021). Coherence between decomposed components of wrist and finger PPG signals by imputing missing features and resolving ambiguous features. *Sensors, 21*(13), 4315. https://doi.org/10.3390/s21134315
Ubbink, D. (2004). Toe blood pressure measurements in patients suspected of leg ischaemia: A new laser doppler device compared with photoplethysmography. *European Journal of Vascular and Endovascular Surgery, 27*(6), 629–634. https://doi.org/10.1016/j.ejvs.2004.01.031
"Vital Signs", Cleveland Clinic, 2022. [Online]. Available: https://my.clevelandclinic.org/health/articles/10881-vital-signs. (accessed Sep 01, 2022).
Voisin, M., Shen, Y., Aliamiri, A., Avati, A., Hannun, A., & Ng, A. Ambulatory atrial fibrillation monitoring using wearable photoplethysmography with deep learning, arXiv.org, 2022. [Online]. Available: 10.48550/arXiv.1811.07774.
Vollmer, M., Bläsing, D., Reiser, J. E., Nisser, M., & Buder, A. (2023). Simultaneous physiological measurements with five devices at different cognitive and physical loads. *PhysioNet*. https://doi.org/10.13026/wce5-fj54
Wan, C., Chen, D., & Yang, J. (2022). Pulse rate estimation from forehead photoplethysmograph signal using RLS adaptive filtering with dynamical reference signal. *Biomedical Signal Processing and Control, 71*, Article 103189. https://doi.org/10.1016/j.bspc.2021.103189
Wang, C., Yang, G., et al. (2021). DiCyc: Gan-based deformation invariant cross-domain information fusion for medical image synthesis. *Information Fusion, 67*, 147–160. https://doi.org/10.1016/j.inffus.2020.10.015
Wang, Z., Liu, W., Wang, Y., & Liu, B. (2022). Agcyclegan: Attention-Guided Cyclegan for Single Underwater Image Restoration. In *ICASSP 2022–2022 IEEE International Conference on Acoustics, Speech, and Signal Processing (ICASSP)* (pp. 2779–2783). https://doi.org/10.1109/ICASSP43922.2022.9746215
Wang, L., et al. (2019). SAR-to-optical image translation using supervised cycle-consistent adversarial networks. *IEEE Access, 7*, 129136–129149. https://doi.org/10.1109/ACCESS.2019.2939649
Williams, D. P., et al. (2019). Heart rate variability and inflammation: A meta-analysis of human studies. *Brain, Behavior, and Immunity, 80*, 219–226. https://doi.org/10.1016/j.bbi.2019.03.009
Wu, C., Chen, L., & Li, D. (2019). A Motion Blurred Image Restoration Algorithm Based on CycleGAN. In *2019 IEEE 14th International Conference on Intelligent Systems and Knowledge Engineering (ISKE)* (pp. 968–973). https://doi.org/10.1109/ISKE47853.2019.9170448
Xu, F., et al. (2021). Classification of left-versus right-hand motor imagery in stroke patients using supplementary data generated by CycleGAN. *IEEE Transactions on Neural Systems and Rehabilitation Engineering, 29*, 2417–2424. https://doi.org/10.1109/TNSRE.2021.3123969
Yang, C., Veiga, C., Rodríguez-Andina, J. J., Fariña, J., Iñiguez, A., & Yin, S. (Nov. 2019). Using PPG signals and wearable devices for atrial fibrillation screening. *IEEE Transactions on Industrial Electronics, 66*(11), 8832–8842. https://doi.org/10.1109/TIE.2018.2889614
Yen, C., Chang, S., & Liao, C. (2022). Estimation of beat-by-beat blood pressure and heart rate from ECG and PPG using a fine-tuned deep CNN model. *IEEE Access, 10*, 85459–85469. https://doi.org/10.1109/access.2022.3195857
Yen, C., Liao, J., & Huang, Y. (2022). Applying a deep learning network in continuous physiological parameter estimation based on photoplethysmography sensor signals. *IEEE Sensors Journal, 22*(1), 385–392. https://doi.org/10.1109/jsen.2021.3126744
Yousef, Q., Reaz, M., & Ali, M. (2022). The analysis of PPG morphology. *Investigating the Effects of Aging on Arterial Compliance*.
Zargari, A. H. A., Aqajari, S. A. H., Khodabandeh, H., Rahmani, A. M., & Kurdahi, F. (2022). An accurate non-accelerometer-based PPG motion artifact removal technique using CycleGAN. *ACM Transactions on Computing for Healthcare*. https://doi.org/10.1145/3563949
Zhang, Z., Pi, Z., & Liu, B. (2015). TROIKA: A general framework for heart rate monitoring using wrist-type photoplethysmographic signals during intensive physical exercise. *IEEE Transactions on Biomedical Engineering, 62*(2), 522–531. https://doi.org/10.1109/tbme.2014.2359372
Zhang, Q., Zhou, D., & Zeng, X. Highly wearable cuff-less blood pressure and heart rate monitoring with single-arm electrocardiogram and photoplethysmogram signals, BioMedical Engineering OnLine, vol. 16, no. 1, 2017, doi: 10.1186/s12938-017-0317-z.
Zhang, H., Zhao, M., Wei, C., Mantini, D., Li, Z., & Liu, Q. (2021). EEGdenoiseNet: A benchmark dataset for deep learning solutions of EEG denoising. *Journal of Neural Engineering, 18*(5), Article 056057. https://doi.org/10.1088/1741-2552/ac2bf8
Zhu, J. -Y., Park, T., Isola, P. & Efros, A. A. Unpaired image-to-image translation using cycle-consistent adversarial networks, 2017 IEEE International Conference on Computer Vision (ICCV), Venice, Italy, 2017, pp. 2242-2251, doi: 10.1109/ICCV.2017.244.